Numerical modeling of the thermal expansion of an energetic material

Andrey Ambos, François Willot, Dominique Jeulin, Hervé Trumel

Numerical modeling of the thermal expansion of an energetic material

Andrey Ambos[a], François Willot[a]*, Dominique Jeulin[a], Hervé Trumel[b],

[a] MINES ParisTech, PSL - Research university, CMM - Centre for Mathematical Morphology, 35, rue St Honoré, F-77300 FONTAINEBLEAU, France

[b] CEA, DAM, Le Ripault, F-37260 MONTS, France

Abstract

The thermoelastic response of a TATB-based pressed explosive is studied using morphological modeling and a numerical Fourier scheme. First, we characterize the polycrystalline-like microstructure in terms of the (2D) granulometry and covariance functions, measured on SEM micrograph images. The granulometry is found to be close to a Rayleigh distribution. Second, we represent the polycrystal by a modified Johnson-Mehl tessellation with time-varying germination-rate, in order to approach the wide size distribution observed on the SEM images. We find excellent agreement between the numerically optimized model and the real material in terms of granulometry. Third, we compute the thermoelastic response of the microstructure model by means of full-field Fourier-based computations. Each crystal is assigned uncorrelated random orientations. The thermomechanical response of single crystals is provided by the molecular dynamic simulations of Bedrov et al. (2009) and the X-ray diffraction results of Kolb et al. (1979). Macroscopic (uniform) temperature or strain loadings are applied along various directions (tension, shear or hydrostatic). We observe strong internal stresses upon heating, owing to the highly anisotropic thermoelastic response of TATB and random crystallographic orientations in the polycrystal. The largest stress and strain gradients are observed at grain boundaries, enforcing the idea that grain boundary fracture is indeed the irreversible mechanism underlying ratchet growth. As a first attempt to account for the plastic binder, a 4-voxels soft interphase is inserted at grain boundaries. This results in a strong softening effect on elastic macroscopic properties.

Keywords Fast Fourier Transform method; Polycrystal; Thermoelasticity; Triclinic anisotropy; Homogenization; Random tessellation models

1 Introduction

Energetic materials are nowadays widely used for military and civil purposes, and exist in a large variety of forms, depending upon their destination. Among them, pressed TATB-based polymer-bonded explosives (PBXs) have the peculiarity of combining a high density of chemical energy and a very high level of safety. These materials contain primarily TATB (1,3,5-triamino-2,4,6-trinitrobenzene), a powerful explosive molecular crystal, and a few percent of a polymer that acts as a binder between TATB particles.

These materials display an irreversible and nonlinear thermo-mechanical response to a variety of macroscopic loadings, such as uniaxial compression or tension, for instance. They are also known to display irreversible dilatancy in response to cyclic slow thermal loading (see, e.g. [1, 2, 3]). Provided that temperature exceeds a characteristic threshold, the specific volume of the material increases after each thermal cycle, and eventually stabilizes after a number of cycles that depends upon the nature of the binder. This phenomenon, known as "ratchet growth" in the community of energetic materials, is also known to occur in a variety of materials, especially polycrystalline graphite, and some ceramics (see [1]).

Although the physical origin of this phenomenology is not yet fully understood, the strongly anisotropic thermoelastic behavior of the TATB crystal is suspected to play a fundamental role [4, 5]. The manufacturing process is such that TATB particles are oriented at random in the pressed material, which is therefore macroscopically isotropic, both in microstructure and properties. However, thermal expansion of the crystalline particles is highly anisotropic, and neighboring particles of different crystallographic orientations should partially impede their respective thermal expansions. The induced internal thermal stresses could in turn trigger microscale irreversible phenomena, such as microcracking, or grain plasticity.

This scenario is only qualitative. Examining it in detail needs a numerical tool operating at the level of the microstructure and deriving macroscopic properties at the

*Corresponding author: `francois.willot@ensmp.fr`. Tel.: +33 1 64 69 48 07, Fax: +33 1 64 69 47 07.

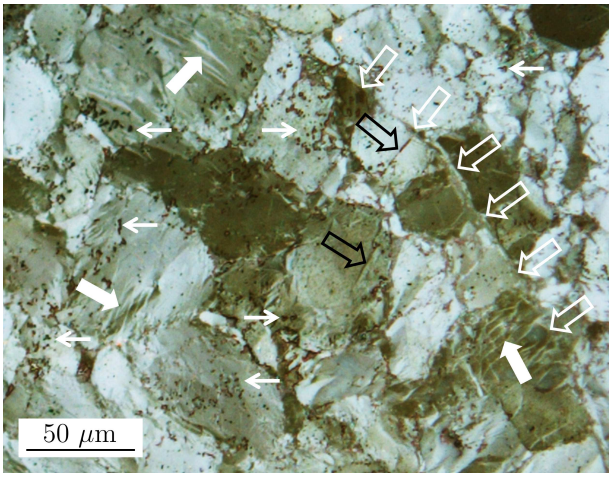

Figure 1: Typical optical microscopy (reflected polarized non analyzed light) micrograph.

same time, in other words a numerical homogenization tool. This in turn requires (i) a description of the microstructure of the studied material, (ii) the knowledge of the behavior of the constituents, including their interfaces, and (iii) a code for performing the simulations.

The present paper reports the first stage of the development of such a tool. Section 2 presents the studied material, its microstructure and its macroscopic behavior and linear thermoelastic properties. Section 3 shows how a model of its microstructure is built, whereas Section 4 deals with the anisotropic behavior of TATB, the major constituent. Section 5 presents the FFT based numerical homogenization method. In section 6, we derive the size of the representative volume element, give the predicted quasi-isotropic thermoelastic macroscopic properties and compare them with available experimental macroscopic data. A first attempt is also made to account for the presence of the polymer binder, treated as a soft interphase at grain boundaries.

Finally, the main results are summarized in the conclusion, which also discusses future work.

2 The material: microstructure and macroscopic thermomechanical response

The material studied here is a pressed TATB-based explosive containing less than 5% of a glassy amorphous polymer. The TATB powder is first coated with the polymer in a slurry process, then granulated to about 1 mm diameter porous spherical prills. The prills are then carefully dried, and isostatically pressed under vacuum at high pressure and moderate temperature in an oil bath, to a final porosity of a few percent.

2.1 Microstructure

Observing the microstructure implies to prepare plane surfaces. However, the material is quite soft, and cutting operations induce heavy damage in a layer down to 1 mm below the surface. Therefore, polishing is required to remove any preparation artifact. Using conventional metallographic tools and procedures, it is relatively easy to prepare flat polished microsections, in a way quite similar to that used for other pressed energetic materials (see, for instance, [6, 7]). The image in Fig. 1 has been obtained using optical reflected polarized (non analyzed) light microscopy.

As expected, the microstructure appears globally as polycrystalline. Individual TATB grains are not easy to recognize, because of very complex contrast patterns. They contain small dark spots (thin white arrows in Fig. 1) and thin band-like features (white solid arrows). The spots are binder-filled pores, remnant of the initial porosity of the TATB powder after the isostatic compaction process. The bands, absent from the initial TATB powder, witness the plastic deformation of individual grains to accommodate compaction. The binder is also supposed to be located at grain boundaries, but cannot be resolved. A few inter- and intra-granular microcracks exist in the material (hollow black arrows), but are not easy to pick from this picture. And finally, the large scale meta-structure corresponding to the remnants of the prills can be observed in the form of a prill bound-

ary (white hollow arrows) crossing the image.

Scanning electron microscopy can also be used to observe polished surfaces. Either in secondary or backscattered electron mode, the contrast is very poor, which presents the advantage of not displaying the deformation bands, but the drawback of not displaying grain boundaries either. This can be improved by etching the surface with a solvent of the binder, since TATB is almost insensitive to common solvents. In this way, grain boundaries can be revealed, as illustrated in Fig. 2.

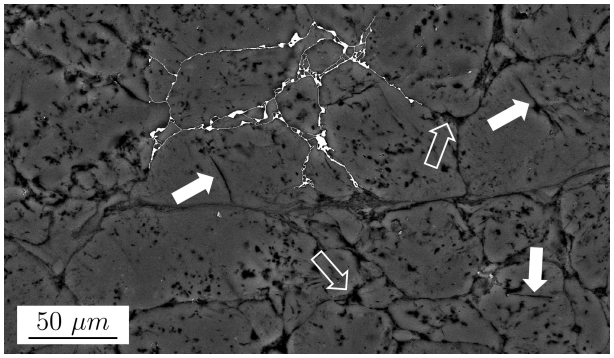

Figure 2: An example of SEM micrograph obtained after etching (resolution: 134 nm per pixel). The deformation bands have disappeared, the binder has been removed from the intra-granular porosity, and some intra-granular cracks are visible.

The dark background is relatively uniform. The grain boundaries are now clearly visible. However, the etching procedure has also removed the binder from the binder-filled porosity, which appears as numerous black spots in all TATB grains. Notice that some grains display intra-granular cracks (white solid arrows in Fig. 2). Some triple points appear hollow (white hollow arrows), which could be due to the etching process removing some of the smallest grains. The thin white network is explained below.

2.2 Segmentation

The remaining porosity represents an artifact, which prevented automatic grain boundary identification and grain segmentation. Therefore, manual segmentation had to be performed on a large polished area (2.55×0.66 mm^2). Two pixel wide lines are drawn following grain boundaries, as illustrated by the white network in Fig. 2. The result is illustrated in Fig. 3.

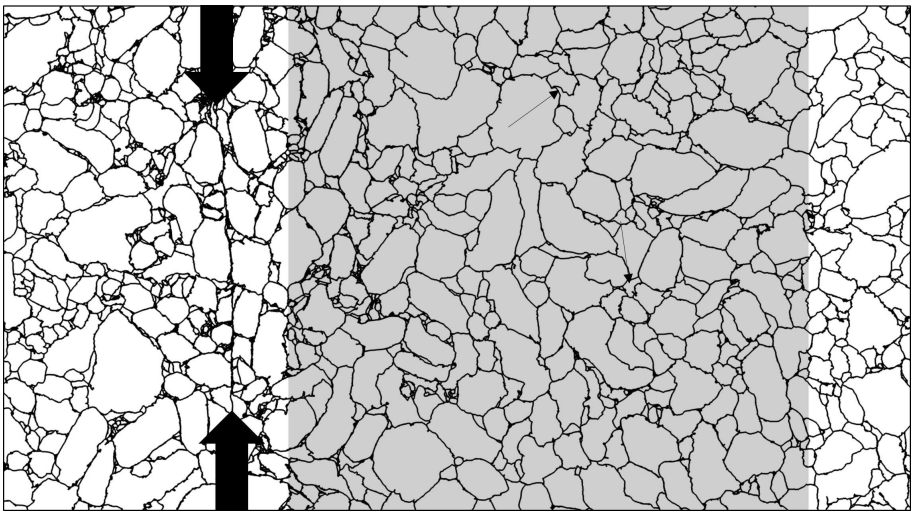

Figure 3: A part of the result of manual segmentation. The grey square corresponds to the magnified image of Fig. 4.

In this image, the intra-granular pores have been deleted, such that only the grain boundaries remain. Many very small grains or intergranular pores are located at grains boundaries or at triple points. It is likely that the etching process has removed a part of the population of micron-sized grains, such that the quantification of the granulometry should be taken with care concerning the smallest grains. Grain boundaries are rough and often concave, whereas grains are noticeably elongated on the average. And finally, the large scale prill metastructure is clearly visible (a prill boundary links the large black arrows in Fig. 3). Clearly, the microstructure is heterogeneous at large (millimetric) scale. The prill boundary zone contains more small grains, and large grains are oriented along the boundary, whereas the bulk prill zone appears isotropic at first sight.

For the present purpose, it is not intended to account for such large scale heterogeneities, but only to demonstrate the feasibility of the approach. Therefore, the study will be restricted to the microstructure representative to the bulk part of the prills (grey square in Fig. 3). Fig. 4 shows this bulk prill zone in more detail, and will constitute the source of morphological data in the following.

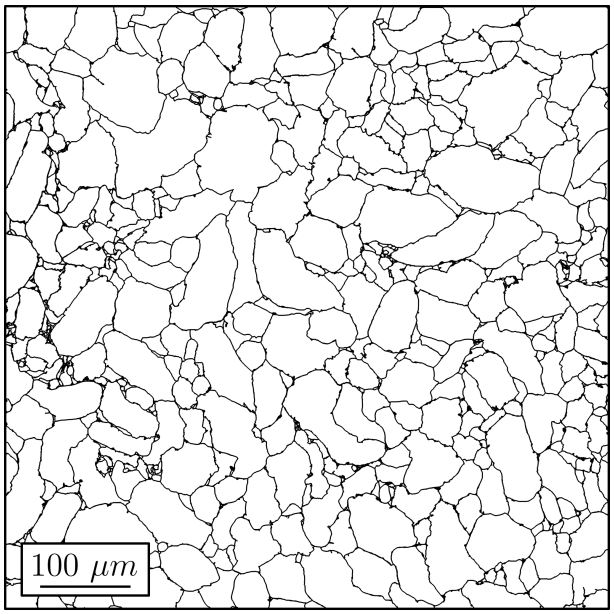

Figure 4: The reference image taken for the remainder of the study (scale : 134 nm per pixel).

Since some of the smallest grains may be missing, the image was submitted to a morphological opening operation with a three pixels diamond element, in order to remove the smallest grains and pores, possibly unrepresentative of the actual microstructure.

2.3 Brief overview of the macroscopic thermomechanical behavior

Fig. 5 shows the result of a cyclic uniaxial compression experiment, performed on a 10 mm diameter, 20 mm length cylindrical sample equipped with longitudinal and transverse strain gauges, at a strain rate of 1.7×10^{-5} s^{-1}. The response is typical of a quasi-brittle (concrete-like) material, damaging progressively up to failure, which occurs around -1.5% longitudinal strain.

Fig. 6 displays the result of a hydrostatic compression cyclic test performed on a 15 mm diameter, 30 mm length cylindrical sample, equipped with longitudinal and transverse gauge as well, at 100 MPa maximum pressure and 1 MPa.s^{-1} stress rate (approximately 4.5×10^{-5} s^{-1} longitudinal strain rate). The response is initially linear, but becomes rapidly compactant, resulting in a -0.4% volumetric residual strain after pressure removal.

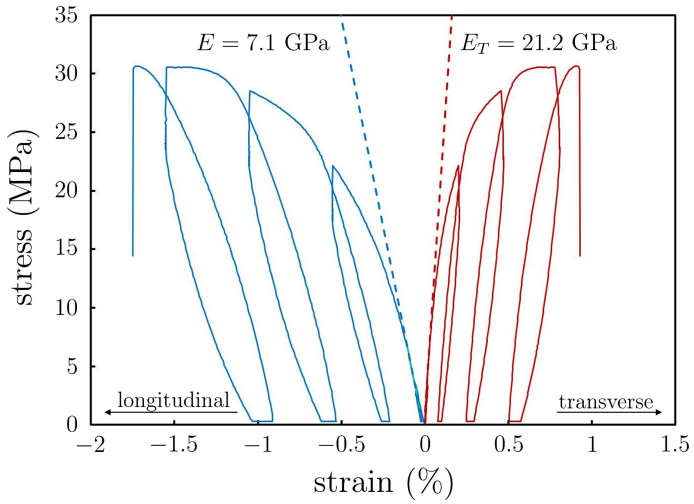

Figure 5: Response to quasi-static cyclic uniaxial compression.

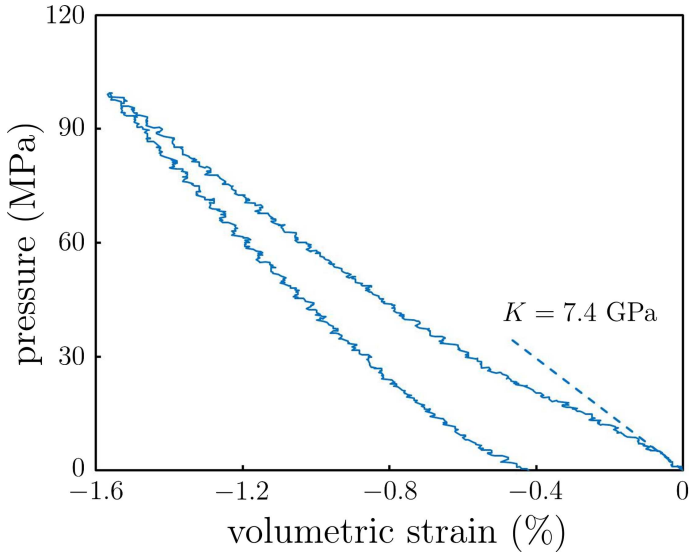

Figure 6: Response to quasi-static cyclic hydrostatic compression.

The macroscopic response to two successive thermal cycles is illustrated in Fig. 7. The sample length is 50 mm and its cross-section is 5×5 mm^2. The plot gives longitudinal deformation versus temperature between ambient temperature and 140°C. The heating/cooling rate is 10°C per hour, which results in quasi-uniform temperature fields in the sample.

Each cycle is characterized by a linear response up to ∼70°C, which corresponds to the glassy domain. After a strongly nonlinear transition phase, linearity is recovered above 120°C. However, this linear phase is irreversible, and accompanied with an irreversible increase of volumetric strain (dilation) of about 0.9 % after the two thermal cycles. Interestingly, the two cooling phases are shifted of about 0.18 % volumetric strain, but can otherwise be superposed. This shows that cooling is reversible, which allows a glass transition temperature to be estimated to 104°C approximately.

2.4 Linear thermoelastic macroscopic properties

From Fig. 5, the Young's and transverse moduli, defined as the initial slopes of the strain-strain curves, can be estimated respectively to 7.1 and 21.2 GPa. Their ratio yields a Poisson's coefficient of 0.335. From these values, a bulk modulus of 7.2 GPa can be deduced. This is reasonably

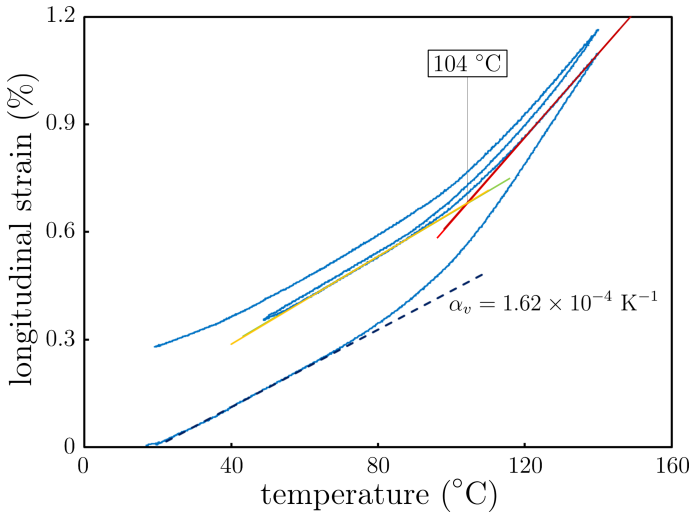

Figure 7: Response to slow thermal cycles.

close to the value deduced from the plot of Fig. 6.

From the data of Fig. 7, a (glassy) volumetric thermal expansion coefficient of $1.62{\times}10^{-4}$ K^{-1} is found. Notice that this value is almost half that of TATB single crystal (see Section 4).

3 Model of microstructure

3.1 Tessellations of space

We now introduce three random tessellation models and use them to simulate the prill bulk zone of the material: the Voronoï, Johnson-Mehl and a modified Johnson-Mehl model described hereafter. Although they bear no relation with the actual manufacturing process of the material, they are in practice efficient for numerical work.

For simplicity, we consider models with as few parameters as possible. Additional degrees of freedom are available, if necessary, as proposed by various authors [8, 9, 10] (see also [11] for much more general space tessellations). Accordingly, the models presented here should be regarded as starting points.

We divide the space $\mathbb{R}^3$ into grains G_i ($i \geq 0$). Each grain is the influence zone of a germ located at point $\mathbf{x_i}$ and appearing at time $t_i \geq 0$:

$$G_i = \left\{\mathbf{x}; |\mathbf{x} - \mathbf{x}^i| + v_0 t_i < |\mathbf{x} - \mathbf{x}^j| + v_0 t_j, \quad j \neq i\right\}. \quad (1)$$

where the growth rate $v_0 = 1$ µm.s^{-1} is the same for all grains and $|\cdot|$ is the Euclidean norm. By convention, time is measured in "seconds" (s) and volume in cubic micrometers (µm^3).

In the Voronoï model, all germs "appear" at the same time, i.e. $t_i \equiv 0$, and the germs $\mathbf{x}^i$ follow a homogeneous Poisson points distribution in $\mathbb{R}^3$. Accordingly, the germs locations have no correlation in space and their spatial distribution depends only on the Poissonian intensity θ (µm^{-3}), or statistical average density of germs per unit of volume. In the Voronoï model, grains are convex polyhedra.

In the Johnson-Mehl model, the points $(\mathbf{x}^i, t_i)$ follow a Poisson distribution in the space $\mathbb{R}^3 \times \mathbb{R}_+$ where $\mathbb{R}_+$ is the set of positive reals. It is prescribed by an intensity θ' (µm^{-3}.s^{-1}). This unique parameter is the average density of appearing germs per unit of time. When θ' is constant, the germs birth rate is constant over time. Note that the Johnson-Mehl model may be equivalently defined by a Poisson distribution of points $\mathbf{x}^i$ in $\mathbb{R}^3$ with intensity θ (µm^{-3}) and a Poisson distribution of times in $\mathbb{R}_+$ of intensity ϕ (s^{-1}). This does not provide additional flexibility as the model depends solely on the product $\theta\phi = \theta'$.

In the Johnson-Mehl model, a crystallized zone "grows" isotropically around each germ, starting at time t_i. Growth is stopped when the crystal meets an adjacent grain. Germs appearing in a zone already crystallized are disregarded. The grain boundaries are quadrics [12] and, contrarily to the Voronoï model, some of the grains are not convex.

In the Johnson-Mehl model, large grains tend to be generated at early germination times, whereas small grains appear lately in the process. Accordingly, an increase of the birth-rate with respect to time leads to broader size distributions in the final tessellations. Indeed, a low germs-density at small times produces large grains. Conversely a high density of germs at the end of the germination process increases the number of small grains. To achieve wider size distributions, we accordingly modify the germs birth-rate ϕ in the Johnson-Mehl model. In this "modified Johnson-Mehl" model we set $\phi = \psi t$, where $\psi > 0$, is a constant. The model's parameters are thus the germs spatial density θ (µm^{-3}), and the rate of increase of the germination rate ψ (s^{-2}).

3.2 Models optimization

For practical purposes, the three Voronoï, Johnson-Mehl and modified Johnson-Mehl models are generated on a cubic 3D grid of size L^3 voxels. We call δ the voxel size in µm. The germs $\mathbf{x}^i$ are generated according to the Poisson intensity θ. In the Johnson-Mehl model, germination times are random variables chosen uniformly in $[0;T]$. The value of T is chosen large enough so that at time T, the entire domain $[0;L]^3$ has crystallized. In practice, we choose arbitrarily one value for T and verify afterwards that the grains cover the whole domain at T; a larger value for T is chosen and the tessellation is recomputed from scratch otherwise. Accordingly, the choice of T does not affect the final tessellation.

Likewise, a maximum germination time T is chosen for the modified Johnson-Mehl model. We let germination times be random variables chosen in $[0;T]$ following the probability density function $P(t)\mathrm{d}t = 2t/T^2\mathrm{d}t$ in the interval $t \in [0;T]$, and $P(t) = 0$ outside. As in the standard Johnson-Mehl model, we verify that all grains cover the whole domain at time T. But contrarily to the standard Johnson-Mehl model, the parameter T affects the final tessellation as the choice of T controls the birth-rate increase rate $\psi = 2/T^2$.

To anticipate on Fourier-based computations, the models are made periodic in space by replicating all germs $\mathbf{x}^i$ at points $\mathbf{x}^i \pm \delta L \mathbf{e}_k$ (k = 1, ..., 3), associated to identical germination times t_i. This amounts to replacing the distance $|\mathbf{x} - \mathbf{x}^i|$ by its periodized version:

$$|\mathbf{x} - \mathbf{x}^i|_{\#} = \sum_{k=1}^{3} \min_{m=0,\pm1} (x_k - x_k^i + m\delta L)^2.$$

We optimize the models's parameters on the granulometry, or grain size distribution, of 2D sections. The cumulative distribution of the granulometry by openings of the set $\mathcal{E} \subset [0;L]^3$ is defined as [13]:

$$G(h) = \frac{P\{\mathbf{x} \in \mathcal{E}\} - P\{\mathbf{x} \in \mathcal{E} \circ S^h)\}}{P\{\mathbf{x} \in \mathcal{E}\}} \qquad (2)$$

where $P\{\mathbf{x} \in \mathcal{E}\} = |\mathcal{E}|/L^3$ is the volume fraction occupied by the set $\mathcal{E}$, and $P\{\mathbf{x} \in \mathcal{E} \circ S^h\}$ that of its morphological opening by the structuring element S^h of size h [13]:

$$\mathcal{E} \circ S_h = \bigcup_{S^h_{\mathbf{x}} \subseteq \mathcal{E}} S^h_{\mathbf{x}}, \quad S^h_{\mathbf{x}} = \{\mathbf{x} + \mathbf{s}; \mathbf{s} \in S^h\}. \qquad (3)$$

We choose a diamond-shaped set S^h for the structuring element so that S^1 is the "cross" $\{(-1;0),(0;0),(0;-1),(0;1),(1;0)\}$. We now choose for $\mathcal{E}$ the interior of the grains, i.e. the whole volume minus the grain boundaries. The grain boundaries are either the segmented SEM image or, on tessellation models, voxels that lie in-between two grains. The latter are defined as voxels having at least two grains in their neighborhood (adjacent voxels). The number of adjacent voxels is set to 4, but this value does not affect the resulting function $G(h)$ (not shown). Finally, to check whether the anisotropy of the structuring element affects the granulometry function $G(h)$ we computed a similar granulometry using a regular octagon as structuring element, which is closer to a disk than the diamond-shaped one we used. We found likewise a very similar granulometry function (not shown).

The granulometry function $G(h)$ of the segmented SEM image is represented in Fig. 8 (black curve). The maximum value for $h \approx 47.4$ µm roughly corresponds to the maximum radius of a circumscribed disk inside the grains. Overall, the function $G(h)$ is close to the one-parameter Rayleigh distribution:

$$G(h) \approx G^r(h) = 1 - \mathbf{e}^{-0.76\left(\frac{h}{h_0}\right)^2}$$

where $h_0 = 18.5\,\mu\mathrm{m}$ is the median of the distribution. This approximation breaks down when considering smaller grains as seen in the log-log plot of $-\log(1-G(h))$ in the inscribed graph in Fig. 8. Indeed, the SEM image exhibits two populations of grains, the smaller one primarily located along the boundaries of large grains and at triple points. This results in the exponent law $-\log(1-G(h)) \simeq h^\beta$ with $\beta < 1$ for small h (see e.g. [14]). Hereafter in this study, small grains are neglected and we fit the tessellation models on the Rayleigh distribution $G^r(h)$ by minimizing the cost functional:

$$\int_{h\geq 0} \mathrm{d}h\, |G^r(h) - G^M(h)|, \qquad (4)$$

where $G^M(h)$ is the granulometry of the Voronoï, standard and modified Johnson-Mehl models.

The size-distribution (estimated from the distribution of areas or volumes of the cells) of the Voronoï model in 2D and 3D closely follows a standard (or, according to some authors, generalized) gamma function fit [15, 16]. Using these results, similar approximations have been proposed for the size-distribution of the Johnson-Mehl model [10]. These approximations break down when considering the granulometry $G^M(h)$ of *2D sections* of 3D models. The slope at the origin of $G^M(h)$, close to 0, is much smaller than that found in gamma fits for the 3D size-distribution. Indeed, large grains will tend to be cut by a random 2D section with higher probability than small grains. Furthermore, no gamma law has been found to fit the 2D size distribution $G^M(h)$ of the Voronoï or Johnson-Mehl models (Fig. 9). Accordingly, in the following, we make use of numerical computations solely.

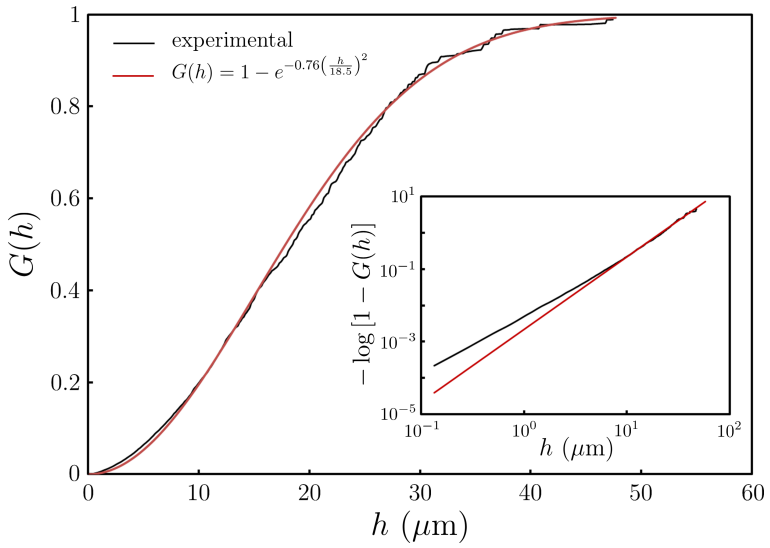

Figure 8: Granulometry by openings $G(h)$ of the reference image (black line) and fit by the cumulative function of a Rayleigh distribution (red line). The value $h_0 = 18.5$ µm is the median size of the granulometry of the reference image. Bottom right, embedded image: log-log plot of the function $-\log(1 - G(h))$.

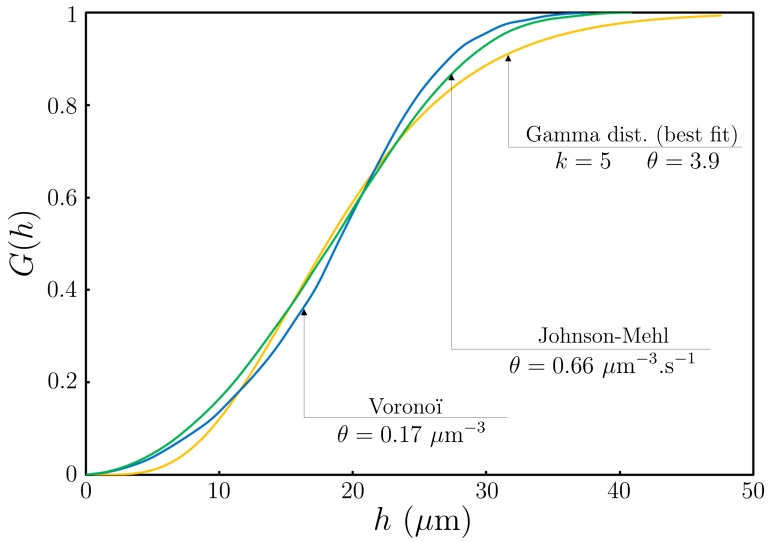

Figure 9: Fit of the 2D-section granulometry of the Voronoï and Johnson-Mehl models with a Gamma distribution $\gamma(\alpha, \beta h)/\Gamma(\alpha)$ of parameters $\alpha = 5.0$, $\beta = 0.26\mu\text{m}^{-1}$.

We optimize the model parameters θ, θ' and $(\theta; T)$ of the Voronoï, standard and modified Johnson-Mehl model to minimize the cost function (4). The size is fixed to $L = 512$ voxels. The first two models are optimized manually, using a dichotomy method. Convergence is obtained after less than 10 steps. The same process is carried out recursively for the modified Johnson-Mehl model, by fixing the first parameter, optimizing on the second, and vice-versa. After about 30 iterations, an optimized model is found. The resulting granulometry functions are represented in Fig. 10. As expected, the granulometry of the Johnson-Mehl model is broader than that of the Voronoï model. Yet, the segmented image exhibits a wider size-distribution than the Johnson-Mehl model can achieve. Only the optimized modified Johnson-Mehl model allows for an accurate fit of the segmented image in terms of granulometry.

2D sections of the optimized models are represented in Fig. 11 and compared with that of the segmented image at the same scale. The images of the models have been enlarged so that only crops of 2D sections are shown. On the 2D section of the modified Johnson-Mehl, one circular

grain is shown embedded in another grain, unlike in the original image (and in other optimized models). Overall, such effects are however extremely rare.

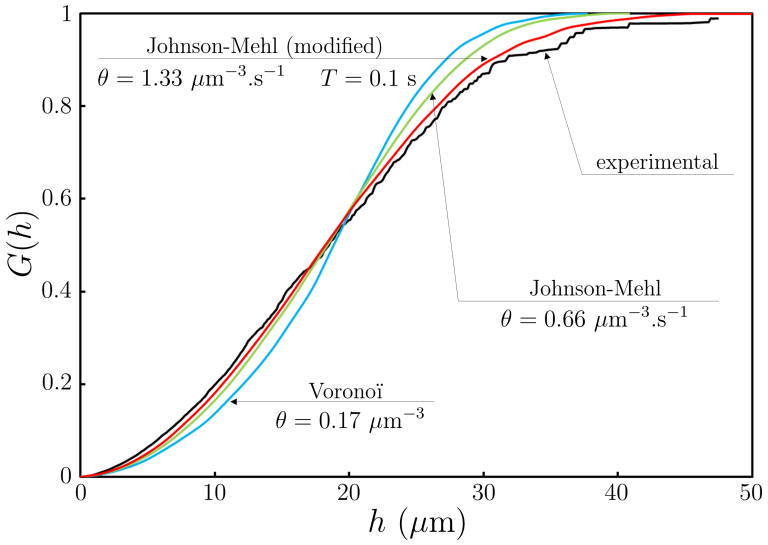

Figure 10: Granulometry by openings $G(h)$ of the reference image (black) and of various optimized models: standard Voronoï and Johnson-Mehl tessellations (blue and green lines respectively) and of the modified Johnson-Mehl model (purple). The granulometry of the models are obtained by averaging over 10 random configurations of size 512^2.

As an additional check, we compared the correlation functions $C(h)$ of the segmented images and of the optimized tessellation models, defined as [17]:

$$C(\mathbf{h}) = \int_{\mathbf{x}} \mathrm{d}^2\mathbf{x}\, \frac{\mathcal{D}(\mathbf{x})\mathcal{D}(\mathbf{x}+\mathbf{h}) - f^2}{f(1-f)} \qquad (5)$$

where the set $\mathcal{D}$ is obtained by coloring randomly each grain in white with probability f and averaging over configurations. Hereafter, we choose $f = 1/2$ and average over 30 random colorings. An example of a random coloring for the modified Johnson-Mehl model is shown in Fig. 12. The resulting function $C(\mathbf{h})$ is nearly isotropic so that we identify $C(\mathbf{h})$ to the function $C(h)$ with $h = |\mathbf{h}|$. Comparisons between the segmented SEM image and the optimized models are represented in Fig. 13. The latter confirms the size of the larger grains of roughly 100 µm in diameter. This is the minimum value of h where $C(h) \approx 0$. At this distance, points separated by h become uncorrelated. Overall the three models fit reasonably well with the correlation function of the SEM segmented image. Hereafter, all computations are carried out on the optimized modified Johnson-Mehl model.

4 Local constitutive behavior

With the above given assumptions about the microstructure, the role of the binder is neglected in a first approximation, and grains properties are supposed homogeneous and purely thermoelastic. Perfect interfaces are assumed. Therefore, all that is needed is the anisotropic thermoelastic properties of the TATB single crystal and the crystallographic orientation of each grain.

Crystallographic data are essentially found in [18]. The TATB crystal is triclinic, with the following lattice parameters : $a = 9.01$ Å, $b = 9.028$ Å, $c = 6.81$ Å, $\alpha = 108.59°$, $\beta = 91.82°$, and $\gamma = 119.97°$, with two molecules per elementary cell. TATB molecules are quasi-planar and assemble together in hydrogen bonded planes, whereas the planes are only bonded by weak van der Waals forces. This peculiar structure explains the very strong anisotropy of the crystal.

Little is found in the specialized literature about the thermoelastic behavior of TATB, but two references provide the required data. The first one [19], consists in a molecular dynamics study of the elastic behavior, as a function of temperature and pressure, and provides the 21 elastic moduli at ambient conditions. The values are given in an orthonormal coordinate system such that the $(\mathbf{x}, \mathbf{y})$ plane coincides with that of the $(\mathbf{a}, \mathbf{b})$ one, and that the $\mathbf{x}$ axis coincides with the $\mathbf{a}$ one (see Appendix). Since these values are derived from an approximate interatomic potential, their accuracy is to be confirmed. The second reference [20], is an experimental X-ray diffraction determination of the variations of the lattice parameters with

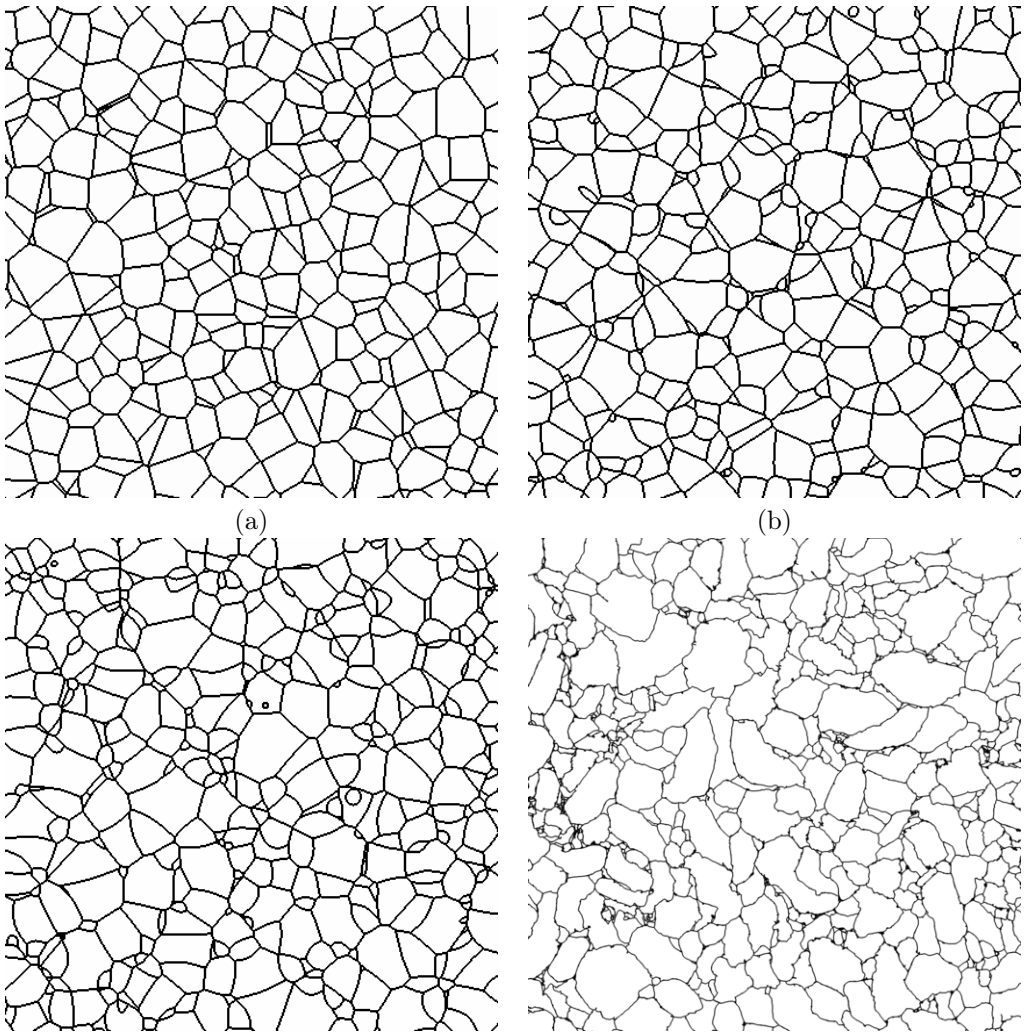

Figure 11: 2D-sections of the Voronoï (a), standard (b) and modified (c) Johnson-Mehl models. The models are optimized to mimic the granulometry of the reference image (d). All images are shown at the same scale.

temperature, in the range [-59;104°C] at ambient pressure. From these values, the components of the thermal expansion tensor can be expressed in the same coordinate system than the elastic tensor (calculations are detailed in the Appendix). Gathering the two results together, we get in the Voigt notation:

$$\begin{pmatrix} \sigma_{xx} \\ \sigma_{yy} \\ \sigma_{zz} \\ \sigma_{yz} \\ \sigma_{xz} \\ \sigma_{xy} \end{pmatrix} = \begin{pmatrix} 65.7 & 18.5 & 4.0 & -0.2 & -1.0 & 1.0 \\ & 62.0 & 5.0 & 0.6 & -0.5 & 1.0 \\ & & 18.3 & 0.2 & -0.4 & -0.4 \\ & & & 1.4 & 0.1 & 0.3 \\ & \text{sym} & & & 0.68 & 0.4 \\ & & & & & 21.6 \end{pmatrix} \times \left[\begin{pmatrix} \varepsilon_{xx} \\ \varepsilon_{yy} \\ \varepsilon_{zz} \\ 2\varepsilon_{yz} \\ 2\varepsilon_{xz} \\ 2\varepsilon_{xy} \end{pmatrix} - \begin{pmatrix} 8.28 \\ 29.04 \\ 264.7 \\ 0.41 \\ -26.14 \\ 3.34 \end{pmatrix} \times 10^{-6} \Delta T \right] \quad (6)$$

where $\boldsymbol{\sigma}$ and $\boldsymbol{\varepsilon}$ are the stress and strain tensors, respectively, and ΔT is the macroscopic temperature loading. Elastic moduli are given in GPa, whereas the components of the thermal expansion tensor are given in K^{-1}. Notice that the thermoelastic behavior, although displaying a triclinic symmetry strictly speaking, is very close to the monoclinic one. The elastic behavior is relatively close to the transverse isotropic symmetry.

5 Thermoelastic response and Fourier numerical method

In this section, we recall the equations of thermoelasticity and present a fast numerical scheme for solving them.

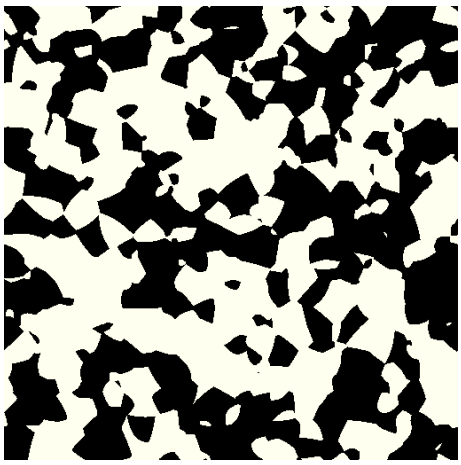

Figure 12: A random coloring of the modified Johnson-Mehl model in Fig. (11c) used to compute the correlation function (Fig. 13).

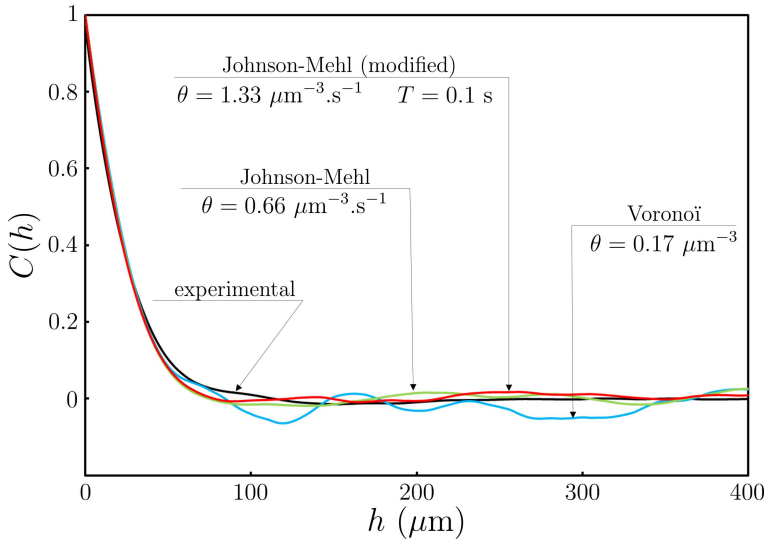

Figure 13: Correlation functions $C(h)$ of the reference image (black) and of various optimized models: standard Voronoï and Johnson-Mehl tessellations (blue and green lines respectively) and modified Johnson-Mehl model (purple). The correlation function of the three models are obtained by averaging over 10 random configurations of size 512^2.

5.1 Thermoelastic behavior

The response of the material is characterized by:

$$\sigma_{ij}(\mathbf{x}) = \widetilde{C}_{ij,kl}(\mathbf{x})\left[\varepsilon_{kl}(\mathbf{x}) - \widetilde{\alpha}_{kl}(\mathbf{x})\Delta T\right] \tag{7}$$

where $\widetilde{\mathbb{C}}(\mathbf{x})$ and $\widetilde{\boldsymbol{\alpha}}(\mathbf{x})$ are the elastic stiffness and thermal expansion tensors of the crystal at point $\mathbf{x}$. They are equal to those in (6) up to a 3D rotation that depends on the lattice directions of the local crystal. We assume the latter are distributed uniformly on the sphere and uncorrelated. The macroscopic temperature loading ΔT is supposed uniform in space. Stress equilibrium and strain admissibility read:

$$\partial_i \sigma_{ij}(\mathbf{x}) \equiv 0, \qquad \varepsilon_{kl}(\mathbf{x}) = (1/2)\left[\partial_l u_k(\mathbf{x}) + \partial_k u_l(\mathbf{x})\right], \tag{8}$$

where $\mathbf{u}(\mathbf{x})$ is the displacement vector at point $\mathbf{x}$. Periodic boundary conditions are applied so that:

$$\boldsymbol{\sigma}\cdot\mathbf{n}\ -\#, \qquad \boldsymbol{\varepsilon}\ \#, \tag{9}$$

where $\mathbf{n}$ is the (outward-pointing) vector normal to the boundary, and $\#$ and $-\#$ stand for periodic and anti-periodic, respectively. Furthermore, we apply a combination of strain and thermal loadings by prescribing the two quantities $\langle\boldsymbol{\varepsilon}\rangle = \overline{\boldsymbol{\varepsilon}}$ and ΔT, where $\langle\cdot\rangle$ is the spatial mean over the computational domain. At the macroscopic level, the effective response of the material is defined by the linear response:

$$\langle\sigma_{ij}(\mathbf{x})\rangle = C_{ij,kl}\left(\overline{\varepsilon}_{kl} - \alpha_{kl}\Delta T\right), \tag{10}$$

where $\mathbb{C}$ is the polycrystal's effective elastic tensor and $\boldsymbol{\alpha}$ its thermal expansion tensor. The volumetric thermal expansion coefficient is $\alpha_v = \mathrm{tr}(\boldsymbol{\alpha}) = \alpha_{11} + \alpha_{22} + \alpha_{33}$. The polycrystal's thermoelastic response (10) is computed by applying different combinations of strain and thermal loadings. Pure strain loading is recovered when $\Delta T = 0$ whereas for purely thermal loading, $\overline{\varepsilon} = 0$.

5.2 Accelerated FFT scheme for thermoelasticity

The "direct" [21] and "accelerated" [22] FFT schemes have been extended to thermoelasticity in [23] More recently, the method in [21] has been modified to compute the stress-free state of a thermoelastic material [24]. In the present work, we use the "accelerated scheme". The latter exhibits higher convergence rates than the "direct scheme", in particular for highly-contrasted composites [23, 25]. An alternative choice to the "accelerated scheme" is the "augmented Lagrangian" scheme [26, 27], useful for media with infinite contrast of properties. Since we neglect porosity, the latter is not mandatory here.

As a rule, FFT methods are based on the Lippman-Schwinger equations. For the thermoelastic problem (7), (8) and (9), they read:

$$\boldsymbol{\varepsilon} = \overline{\boldsymbol{\varepsilon}} - \mathbb{G}^0 * \boldsymbol{\tau}, \quad \boldsymbol{\tau} = \boldsymbol{\sigma} - \mathbb{C}^0 : \boldsymbol{\varepsilon} = \left(\widetilde{\mathbb{C}} - \mathbb{C}^0\right) : \boldsymbol{\varepsilon} - \widetilde{\mathbb{C}} : \widetilde{\boldsymbol{\alpha}} \Delta T \tag{11}$$

where $\mathbb{C}^0$ is an arbitrary homogeneous stiffness tensor, $\boldsymbol{\tau}$ its associated polarization field and $\mathbb{G}^0$ is the Green operator associated to $\mathbb{C}^0$, of zero mean. Double contractions and convolution products are represented by a colon (:) and the asterisk symbol ($*$), respectively. The accelerated scheme consists in the following iterations for the strain field [23]:

$$\boldsymbol{\varepsilon}^{k+1} = \left(\widetilde{\mathbb{C}} + \mathbb{C}^0\right)^{-1} : \Big\{ 2\mathbb{C}^0 : \overline{\boldsymbol{\varepsilon}} + \widetilde{\mathbb{C}} : \widetilde{\boldsymbol{\alpha}} \Delta T + \left[\delta(\mathbf{x})\mathbb{I} - 2\mathbb{C}^0 : \mathbb{G}^0\right] * \left[\left(\widetilde{\mathbb{C}} - \mathbb{C}^0\right) : \boldsymbol{\varepsilon}^k - \widetilde{\mathbb{C}} : \widetilde{\boldsymbol{\alpha}} \Delta T \right] \Big\}. \tag{12}$$

We initialize the field by setting $\boldsymbol{\varepsilon}^{k=0} \equiv \overline{\boldsymbol{\varepsilon}}$. and monitor the convergence of the algorithm using stress equilibrium as criterion. In the Fourier domain, the operator ∂_i amounts to a multiplication by the component q_i of the Fourier wave vector $\mathbf{q}$. Accordingly, we enforce:

$$\max_{j,\,\mathbf{q}} |q_i \sigma_{ij}(\mathbf{q})| < \eta \max_{i,\,j,\,\mathbf{q}=0} |\sigma_{ij}(\mathbf{q})| = \eta \max_{i,\,j} |\langle \sigma_{ij}(\mathbf{x}) \rangle| \,,$$

where $\sigma_{ij}(\mathbf{q})$ is the Fourier transform of $\sigma_{ij}(\mathbf{x})$ and η is the error tolerance. We choose $\eta = 10^{-8}$. Additional CPU and storage are required to compute the error criterion. To minimize this effect, we compute it once every ten iterations.

The convergence of the FFT algorithm depends strongly on the choice for the homogeneous tensor $\mathbb{C}^0$. For simplicity, we restrict ourselves to isotropic tensors $\mathbb{C}^0$ defined by a shear modulus μ^0 and bulk modulus κ^0. For binary media with two isotropic phases $(\mu^\beta, \kappa^\beta)_{\beta=1,2}$, it has been shown that the following choice is optimal [27, 25]:

$$\mu^0 = \sqrt{\mu^1 \mu^2}, \qquad \kappa^0 = \sqrt{\kappa^1 \kappa^2}.$$

This, however, does not apply to polycrystals, and so we explore numerically varying values of μ^0 and κ^0. For our model material, the scheme will not converge for small values of μ^0 and κ^0 such as $\mu^0 = \kappa^0 = 1$ GPa. Convergence is obtained only by increasing the moduli. It was found to be roughly optimal for $\mu^0 = \kappa^0 = 10$ GPa. In all computations carried out hereafter, the number of iterations was less than 50.

6 Thermoelastic response of the polycrystal

6.1 Field distributions

We compute the full-field thermoelastic response of the optimized modified Johnson-Mehl model discretized on a grid of 1024^3 voxels. We apply a purely thermal loading $\Delta T = 1$ and three purely elastic loadings: hydrostatic strain loading $\overline{\varepsilon}_m = \overline{\varepsilon}_{kk}/3 = 1$, tension along x, $\overline{\varepsilon}_{xx} = 1$ and shear along y and z, $\overline{\varepsilon}_{yz} = 1/2$. The histograms $P_{\sigma_{ij}}(t)$ and $P_{\varepsilon_{ij}}(t)$ of the stress and strain components are represented in Fig. 14 for thermal and hydrostatic loadings and in Fig. 15 for the tension and shear loadings.

The latter are formally defined as:

$$\begin{aligned} P_{\sigma_{ij}}(t) &= \int_{\mathbf{x}} \mathrm{d}^3\mathbf{x}\, \delta(t - \sigma_{ij}(\mathbf{x})), \\ P_{\varepsilon_{ij}}(t) &= \int_{\mathbf{x}} \mathrm{d}^3\mathbf{x}\, \delta(t - \varepsilon_{ij}(\mathbf{x})). \end{aligned}$$

Accordingly, $P_{\sigma_{ij}}(t)\mathrm{d}t$ (resp. $P_{\varepsilon_{ij}}(t)\mathrm{d}t$) is the probability that $\sigma_{ij}(\mathbf{x})$ (resp. $\varepsilon_{ij}(\mathbf{x})$) is comprised in the range $[t; t + \mathrm{d}t]$. We also compute histograms of the Von Mises equivalent strain and stress fields:

$$\begin{aligned} \varepsilon_{\mathrm{eq}}(\mathbf{x}) &= \sqrt{(2/3)\boldsymbol{\varepsilon}'(\mathbf{x}) : \boldsymbol{\varepsilon}'(\mathbf{x})}, & (13) \\ \sigma_{\mathrm{eq}}(\mathbf{x}) &= \sqrt{(3/2)\boldsymbol{\sigma}'(\mathbf{x}) : \boldsymbol{\sigma}'(\mathbf{x})}, & (14) \\ \boldsymbol{\varepsilon}'(\mathbf{x}) &= \boldsymbol{\varepsilon}(\mathbf{x}) - \varepsilon_m(\mathbf{x})\delta_{ij}, \quad \boldsymbol{\sigma}'(\mathbf{x}) = \boldsymbol{\sigma}(\mathbf{x}) - \sigma_m(\mathbf{x})\delta_{ij}, \end{aligned}$$

with $\varepsilon_m = \varepsilon_{kk}/3$, $\sigma_m = \sigma_{kk}/3$. For hydrostatic strain loadings and thermal loading, the shear components $\varepsilon_{xy,xz,yz}$ and $\sigma_{xy,xz,yz}$ have zero mean and are symmetrical with respect to 0. This does not hold for the other components. The dilatational strain components $\varepsilon_{xx,yy,zz}$, in particular, display a change of convexity. The mean strain and stress components, however, show a nearly-Gaussian distribution, except when approaching the tail of the distribution. These remarks also hold when tensile loading is applied (Fig. 15).

The results above do not necessarily depend on the geometric model chosen for the polycrystal. In a previous work based on finite element computations [28], the elastic and plastic strain and stress fields occuring in the 3D Poisson-Voronoï model and in a simplified model with cubic-shaped grains have been computed. Slightly broader field distributions have been predicted for polyhedric grains rather than cubic grains, but overall the strain and stress histograms for the two geometries are very close to one another. The effect of the choice of the tesselation model for the TATB material on the fields distribution, outside of the present study, will be investigated in a future work. In any case, accurate modeling of the polycrystal geometry is presumably important to incorporate the effect of the binder, to predict strain field localization or fracture [28].

6.2 Local fields

2D sections of the mean stress σ_m and equivalent strain and stress fields are represented in Fig. 16, for hydrostatic compression and thermal loading. The same fields are represented in Fig. 17 for tensile and shear loading. Only one quarter of the full 2D section, of size 512×512 voxels, is shown. Some numerical artifacts are visible, in the form of oscillations (tantamount to Gibbs' effect), for instance in the map for the mean stress component σ_m under thermal loading. These effects are a consequence of the underlying discretization used in the Fourier method [29].

Overall, highest values for the equivalent strain field ε_{eq} preferentially occur along the grains edges, and, in particular, near corners. The equivalent stress field σ_{eq} shows the same tendency, whereas the mean strain and stress components ε_m and σ_m are less localized. For shear loading $\overline{\varepsilon}_{yz} = 1/2$, the fluctuations of the mean stress field σ_m are lower than the equivalent strain and stress fields.

6.3 Effective response

We now compute the effective elastic and thermal expansion tensors by applying strain loadings along 6 independent directions $\overline{\varepsilon}_{ij} = 1$ $(i \leq j)$ as well as thermal loading with no deformation $\Delta T = 1$, $\overline{\boldsymbol{\varepsilon}} = \mathbf{0}$. The effective strain-stress relation read, in Voigt notation:

$$\begin{pmatrix} \langle\sigma_{xx}\rangle \\ \langle\sigma_{yy}\rangle \\ \langle\sigma_{zz}\rangle \\ \langle\sigma_{yz}\rangle \\ \langle\sigma_{xz} \\ \langle\sigma_{xy}\rangle \end{pmatrix} = \begin{pmatrix} 26.81 & 12.42 & 12.33 & -0.027 & 0.137 & -0.016 \\ 12.40 & 26.64 & 12.20 & 0.194 & -0.069 & 0.074 \\ 12.35 & 12.25 & 27.07 & 0.029 & 0.048 & -0.054 \\ 0.030 & 0.213 & 0.066 & 7.788 & -0.017 & -0.002 \\ 0.142 & -0.062 & 0.053 & 0.006 & 7.969 & 0.043 \\ -0.011 & 0.060 & -0.046 & -0.008 & 0.020 & 7.873 \end{pmatrix} \times \left[\begin{pmatrix} \overline{\varepsilon}_{xx} \\ \overline{\varepsilon}_{yy} \\ \overline{\varepsilon}_{zz} \\ 2\overline{\varepsilon}_{yz} \\ 2\overline{\varepsilon}_{xz} \\ 2\overline{\varepsilon}_{xy} \end{pmatrix} - \begin{pmatrix} 8.254 \\ 8.489 \\ 8.243 \\ -0.131 \\ -0.108 \\ -0.992 \end{pmatrix} \times 10^{-5} \Delta T \right] \tag{15}$$

As expected, the effective elastic tensor $\mathbb{C}$ in the relation above is nearly isotropic, since we chose uncorrelated crystal orientations in all directions. We identify it with an isotropic tensor $\mathbb{C}^{\text{iso}}$ of bulk and shear moduli κ and μ, by minimizing:

$$\inf_{\kappa,\mu} \left\{ \frac{\sum_{i,j} |C_{ij} - C_{ij}^{\text{iso}}(\kappa,\mu)|}{\max_{i,j} |C_{ij}|} \right\}. \tag{16}$$

We find $\kappa = 17.2$ and $\mu = 7.4$ GPa for the bulk and shear moduli of the polycrystal, respectively, and $\alpha_v = 2.50\,10^{-4}\ K^{-1}$ for the volumetric thermal expansion coefficient. In next section, we estimate the relative accuracy of these results.

6.4 Representative volume element

We first examine the effect of discretization on a voxel grid, or resolution. To check our result's sensitivity with respect to resolution, we perform similar computations on a microstructure model discretized on a coarser grid of 512^3 voxels. Both the 1024^3 and 512^3 model contain about $12,000$ grains, but the germs and apparition times are different in the two models. The resolution in the 512^3 images is 1.57 µm per voxel and 785 nm per voxel in the 1024^3 image. Results for the 512^3 voxels grid yield:

$$\begin{pmatrix} \langle\sigma_{xx}\rangle \\ \langle\sigma_{yy}\rangle \\ \langle\sigma_{zz}\rangle \\ \langle\sigma_{yz}\rangle \\ \langle\sigma_{xz} \\ \langle\sigma_{xy}\rangle \end{pmatrix} = \begin{pmatrix} 26.80 & 12.42 & 12.33 & -0.027 & 0.137 & -0.015 \\ 12.40 & 26.63 & 12.20 & 0.194 & -0.069 & 0.074 \\ 12.35 & 12.25 & 27.07 & 0.029 & 0.048 & -0.053 \\ 0.030 & 0.213 & 0.066 & 7.787 & -0.017 & -0.002 \\ 0.142 & -0.063 & 0.053 & 0.006 & 7.967 & 0.043 \\ -0.010 & 0.061 & -0.045 & -0.008 & 0.020 & 7.871 \end{pmatrix}$$

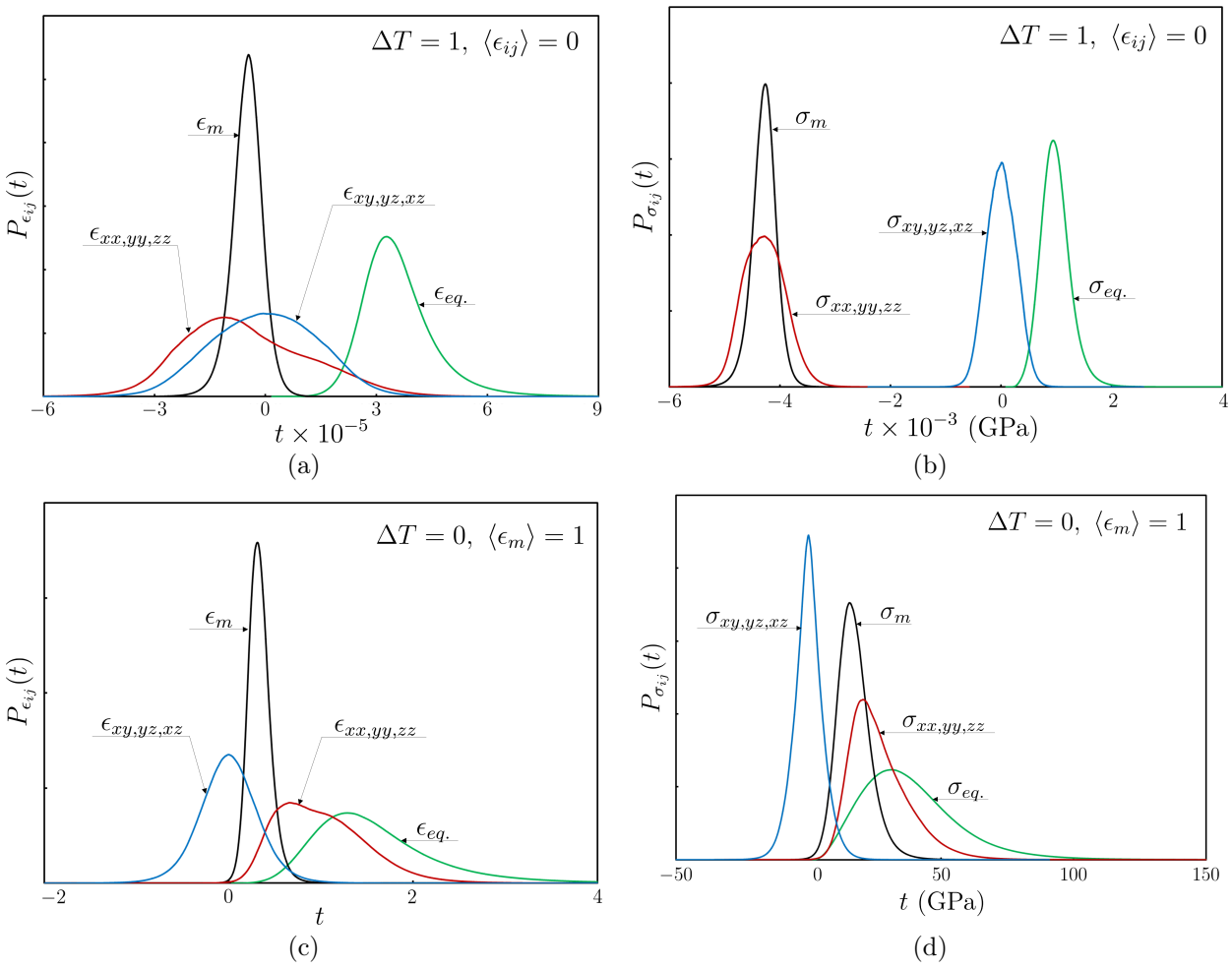

Figure 14: Strain (a,c) and stress (b,d) field histograms computed on a system of size 1024^3 voxels. Each histogram is normalized such that $\int_{-\infty}^{+\infty} P(t)dt = 1$. Thermal loading $\Delta T = 1$, $\langle \varepsilon_{ij} \rangle = 0$ (a,b) and hydrostatic strain loading $\langle \varepsilon_m \rangle = 1$, $\Delta T = 0$ (c,d) are applied.

$$\times \left[\begin{pmatrix} \bar{\varepsilon}_{xx} \\ \bar{\varepsilon}_{yy} \\ \bar{\varepsilon}_{zz} \\ 2\bar{\varepsilon}_{yz} \\ 2\bar{\varepsilon}_{xz} \\ 2\bar{\varepsilon}_{xy} \end{pmatrix} - \begin{pmatrix} 8.253 \\ 8.487 \\ 8.242 \\ -0.102 \\ -0.036 \\ -0.028 \end{pmatrix} \times 10^{-5} \Delta T \right]. \tag{17}$$

We recover the same effective estimates up to small corrections. Furthermore, the error (16) with respect to isotropy is equal to 0.4% for both grids. Resolution has therefore little impact on the effective properties. Note that these results concern the effective properties only. Local fields are generally more sensitive to resolution than the macroscopic properties, typically along grain boundaries [24] (see also [29] in another context).

We now examine the representativeness of the model, i.e. the statistical accuracy of the estimates for the polycrystal properties with respect to the number of grains. Recall that the apparent elastic moduli and thermal coefficients are computed by taking averages over the stress tensor field. Since the latter is a stationary and ergodic random function in space, it follows that [30]:

$$\frac{D^2_{\sigma_{ij}}(V)}{D^2_{\sigma_{ij}}} \sim \frac{A_3^{\sigma_{ij}}}{V}, \quad V \gg A_3^{\sigma_{ij}}, \tag{18}$$

where $A_3^{\sigma_{ij}}$ (μm^3) is the integral range for the field σ_{ij}, $D^2_{\sigma_{ij}}(V)$ is the variance of the spatial means $\langle \sigma_{ij}(\mathbf{x}) \rangle_V$ computed on a volume V, and $D^2_{\sigma_{ij}}$ is the point variance of the field $\sigma_{ij}(\mathbf{x})$, i.e.:

$$D^2_{\sigma_{ij}} = \langle \sigma^2_{ij} \rangle - \langle \sigma_{ij} \rangle^2.$$

With $N = V/A_3^{\sigma_{ij}} \gg 1$, relation (18) reads $D^2_{\sigma_{ij}}(V) \sim D^2_{\sigma_{ij}}/N$ so that, in terms of fluctuations, V acts as N independent subvolumes of size $A_3^{\sigma_{ij}}$.

Expression (18) allows one to estimate the size of the representative volume element V_{RVE} with respect to the

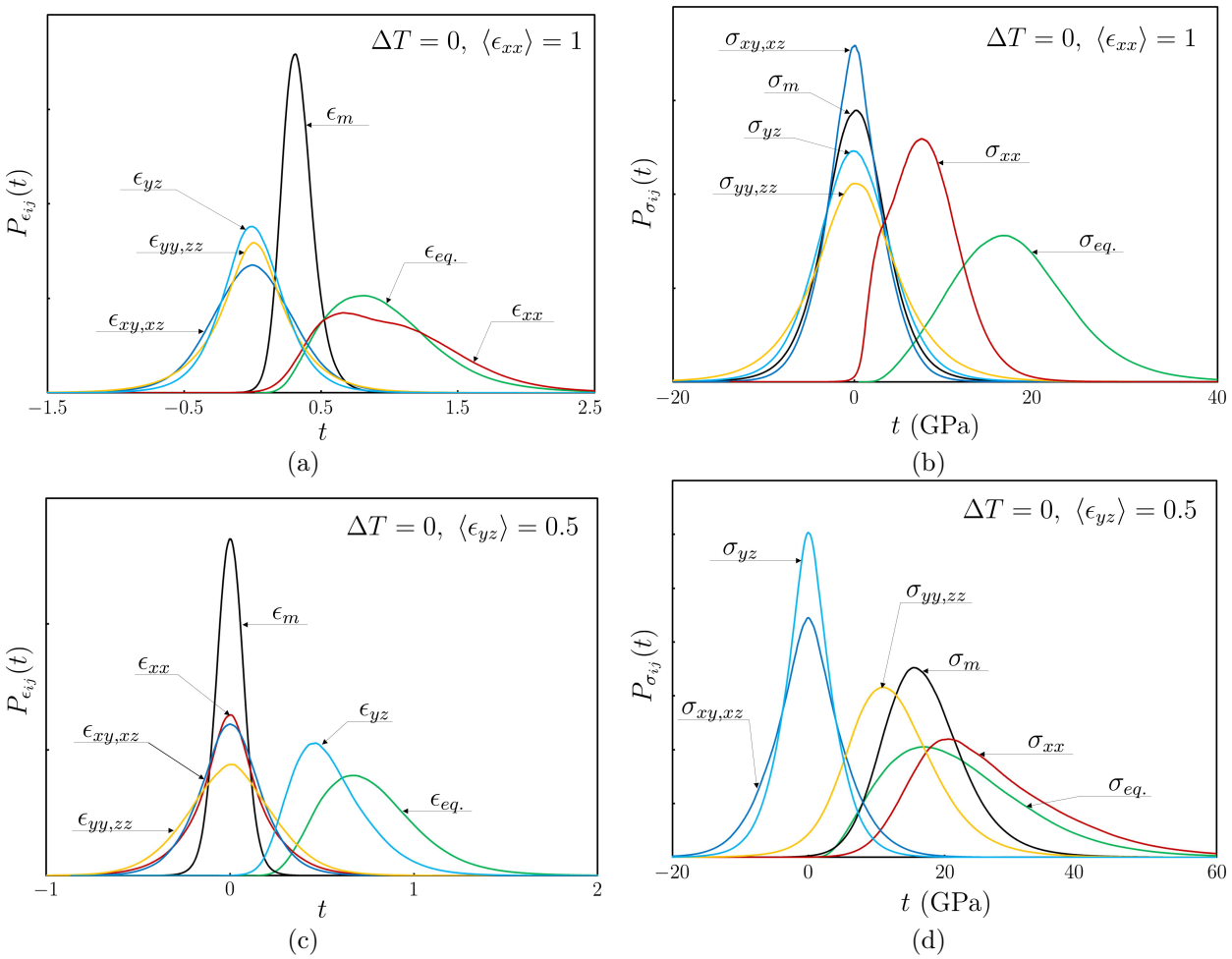

Figure 15: Strain (a,c) and stress (c,d) field histograms computed on a system of size 1024^3 voxels. Tension along the x direction $\langle \varepsilon_{xx} \rangle = 1$ (a,b) and shear loading along the y, z plane $\langle \varepsilon_{yz} \rangle = 1/2$ (c,d) is applied.

requested accuracy ϵ^2 as:

$$V_{RVE} = \frac{4 D^2_{\sigma_{ij}} A_3^{\sigma_{ij}}}{\epsilon^2 \langle \sigma_{ij} \rangle^2}, \tag{19}$$

when $V \gg A_3^{\sigma_{ij}}$. As a consequence of the term $1/\epsilon^2$ on the right-hand side, the RVE size increases strongly when ϵ decreases. To increase the accuracy by an order of magnitude, the size of the RVE has to be multiplied by about 4.6. For instance, if we assume a volume containing 512^3 voxels gives a result accurate up to the n-th digit, a volume of about 2350^3 voxels is necessary for computing the $(n+1)$-th digit.

Hereafter, we introduce the variances $D^2_\kappa(V)$ and $D^2_{\alpha_v}(V)$, computed on the fields σ_m with different loading conditions: hydrostatic strain loading $\overline{\varepsilon}_m = 1$ with no thermal loading $\Delta T = 0$, for $D^2_\kappa(V)$, and purely-thermal loading $\Delta T = 1$, $\overline{\varepsilon} = 0$ respectively. We also introduce $D^2_\mu(V)$, the variance of the means of the field σ_{yz} when shear loading $\overline{\varepsilon}_{yz} = 0.5$ and $\Delta T = 0$ is applied. We computed the three variances using one configuration of size 1024^3, that we divided into a set of non-overlapping cubic subvolumes of length $\ell = V^{1/3}$, for increasing values of $\ell = 1$, ..., 512 (in number of voxels) or $\ell = 0.785$, ..., 402 (in µm). The three variances, normalized by the point variances D^2_κ, $D^2_{\alpha_v}$ and D^2_μ, are represented in Fig. 18. For small values of ℓ, the volume V is less than the integral range ($V < A_{\sigma_{ij}}$) and the asymptotic expansion 18 does not hold. On the contrary, when $\ell \lesssim 400$ µm, estimates of the variances are not accurate because of the small number of subvolumes, equal to 8. In an intermediate regime of about one and a half decade for κ and one decade for α_v we find the asymptotic expansions:

$$\frac{D^2_\kappa(\ell)}{D^2_\kappa} \sim \frac{A_3^\kappa}{\ell^3}, \quad \frac{D^2_{\alpha_v}(\ell)}{D^2_{\alpha_v}} \sim \frac{A_3^{\alpha_v}}{\ell^3}, \tag{20}$$

where the point variances are $D^2_\kappa \approx 200.6$ GPa^2, $D^2_{\alpha_v} \approx 6.7\,10^{-6}$ GPa^2 and the corresponding integral ranges equal $A_3^\kappa \approx 38^3$ µm^3 and $A_3^{\alpha_v} \approx 45^3$ µm^3. On the 1024^3 system size, $A_3^\kappa = 49^3$ voxels and $A_3^{\alpha_v} = 57^3$ voxels. The relative accuracy ϵ_κ of the estimate for the bulk modulus κ as a

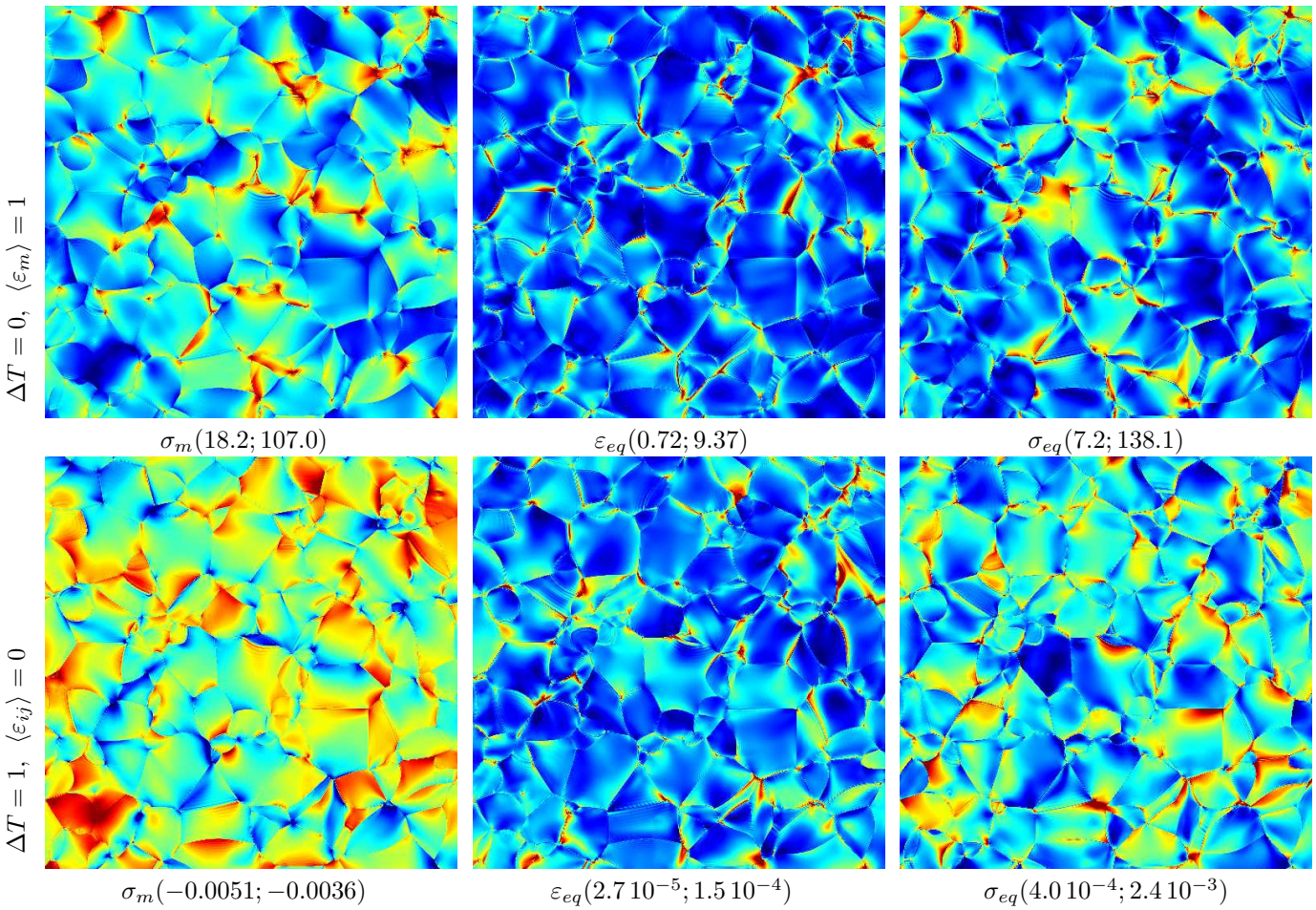

Figure 16: 2D sections of the mean stress σ_m, Von Mises equivalent strain ε_{eq} and stress fields σ_{eq} (left to right), with applied hydrostatic strain loading $\langle \varepsilon_m \rangle = 1$, $\Delta T = 0$ (top) and thermal loading $\Delta T = 1$, $\langle \varepsilon_m \rangle = 0$ (bottom). The x axis is oriented top to bottom and the y axis left to right. To highlight the field patterns, the highest and lowest 0.3% values are thresholded. The resulting threshold values are indicated between brackets. Lowest and highest values are shown in blue and red resp. with green and yellow in-between. One quarter (512×512 voxels) of the complete system (1024×1024 voxels) is represented.

function of ℓ is given by Eqs. 19 and 20:

$$\epsilon_\kappa = \frac{2D_\kappa \sqrt{A_3^\kappa}}{3\kappa} \frac{1}{\ell^{3/2}} \tag{21}$$

For pure-thermal loading $\overline{\boldsymbol{\varepsilon}} = 0$, $\Delta T = 1$, the volumetric thermal expansion is $\alpha_v = -\langle \sigma_m \rangle / \kappa$. Accordingly, the relative accuracy for the volumetric thermal expansion is:

$$\epsilon_{\alpha_v} = \left(\frac{2D_{\alpha_v} \sqrt{A_3^{\alpha_v}}}{\alpha_v \kappa} + \frac{2D_\kappa \sqrt{A_3^\kappa}}{3\kappa} \right) \frac{1}{\ell^{3/2}} \tag{22}$$

For the 1024^3 system:

$$\epsilon_\kappa \approx 0.6\%, \qquad \epsilon_{\alpha_v} \approx 2.2\%, \tag{23}$$

i.e. $\kappa = 17.2 \pm 0.1$ GPa and $\alpha_v = 2.50\,10^{-4} \pm 0.06\,10^{-4}$ K^{-1}. Conversely, a system size of 2.5 mm containing about 38000 grains (3250^3 voxels at the resolution employed here) would be necessary to achieve a accuracy of 0.1% on the bulk modulus. The same relative accuracy for the thermal expansion would require a volume of size 6.2 mm containing about 5.6 million grains (7940^3 voxels at the resolution employed here).

Regarding the shear modulus μ, data are insufficient to obtain an asymptotic fit of $D_\mu^2(\ell)$ as in Eq. 20. However, we find that $D_\mu^2(\ell)/D_\mu^2 \approx 1.58\,10^{-3}$ for $\ell = 402$ µm, which allows to compute the relative precision of our computation as

$$\epsilon_\mu \approx 0.5\%, \tag{24}$$

i.e. $\mu = 7.40 \pm 0.04$ GPa.

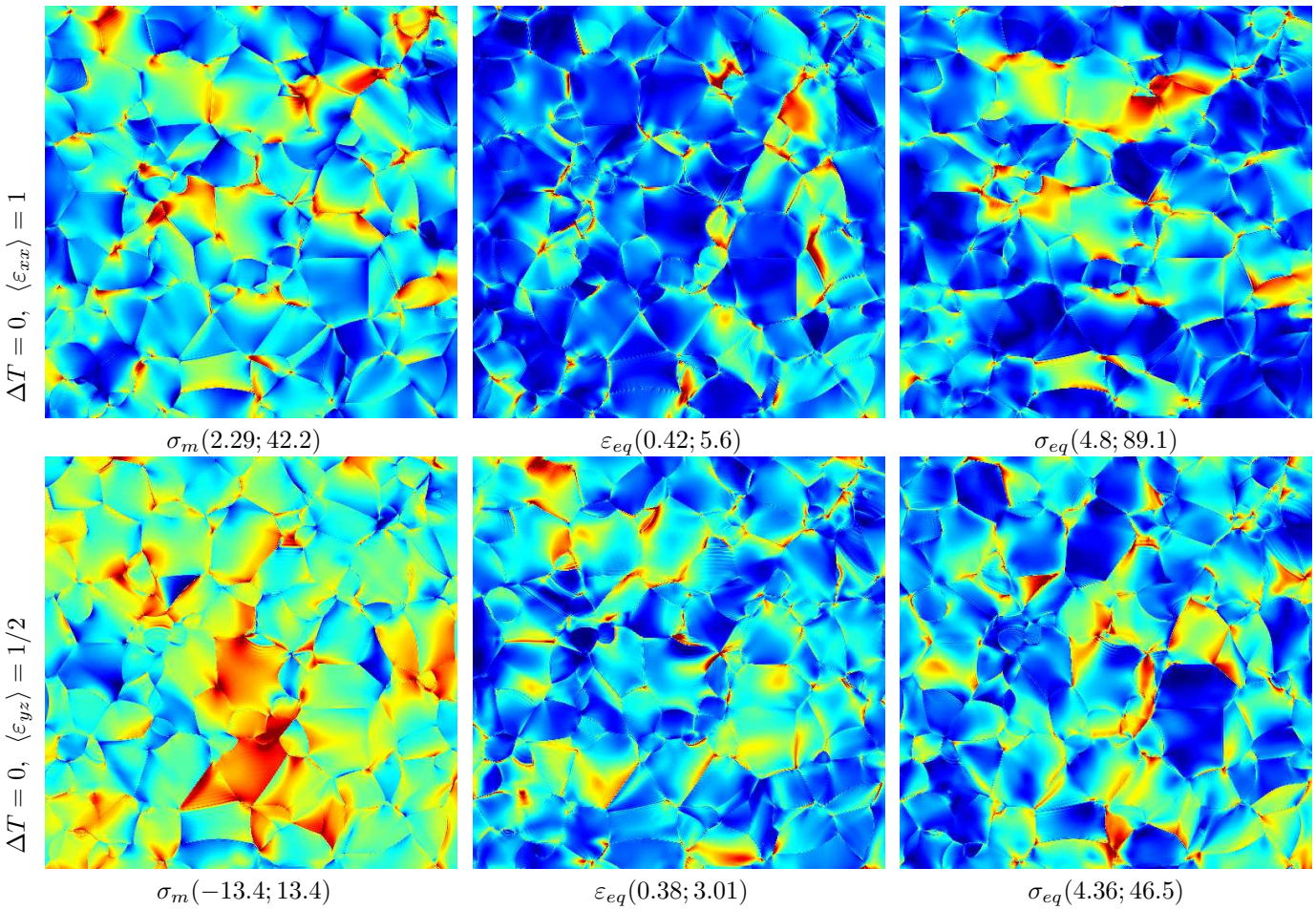

Figure 17: 2D sections of the mean stress σ_m, Von Mises equivalent strain ε_{eq} and stress fields σ_{eq} (left to right), with applied strain tensile loading $\langle \varepsilon_{xx} \rangle = 1$, $\Delta T = 0$ (top) and shear strain loading $\langle \varepsilon_{yz} \rangle = 1/2$ (bottom). The x axis is oriented top to bottom and the y axis left to right. To highlight the field patterns, the highest and lowest 0.3% field values are thresholded. The resulting threshold values are indicated between brackets. Lowest and highest values are shown in blue and red respectively with green and yellow in-between. One quarter (512×512 voxels) of the complete system (1024×1024 voxels) is represented.

6.5 Analytical bounds

We now compare FFT results for the thermal expansion coefficient α_v and bulk modulus κ with available analytical bounds (Fig. 19). For polycrystals with full triclinic anisotropy, Gibiansky and Torquato. [31] give an upper and lower bound for α_v that depend on the value of κ (note that it does not depend on μ). The latter extend bounds previously given in the context of composites with isotropic phases [32, 33]. The bulk modulus is itself comprised between Hill's lower and upper bounds [34]. The two bounds in [31] accordingly delimit a region of acceptable values for α_v and κ in α_v-κ coordinates system.

The bounds are complemented with two sets of upper and lower bounds for the bulk modulus and the thermal expansion coefficient [35]. These bounds, which are narrower than Hill's bounds, are valid when the monocrystal's elastic tensor follows the hexagonal symmetry. To compute these bounds, we approximate the TATB monocrystal by a transversely isotropic elastic tensor, which reads, in Voigt notation:

$$\begin{pmatrix} 63.85 & 18.5 & 4.5 & 0 & 0 & 0 \\ & 63.85 & 4.5 & 0 & 0 & 0 \\ & & 18.3 & 0 & 0 & 0 \\ & & & 1.04 & 0 & 0 \\ & \text{sym} & & & 1.04 & 0 \\ & & & & & 21.6 \end{pmatrix} \quad (25)$$

The two sets of bounds in [35] are the "third-order" bounds and the narrower "T-matrix" bounds, that extend previous works [36, 37]. They form rectangular regions.

As expected, FFT results lay between the Gibiansky-Torquato bounds, which are valid for arbitrary crystal anisotropy. The FFT estimates are close to the upper bound. The TATB crystal is not strictly-speaking trans-

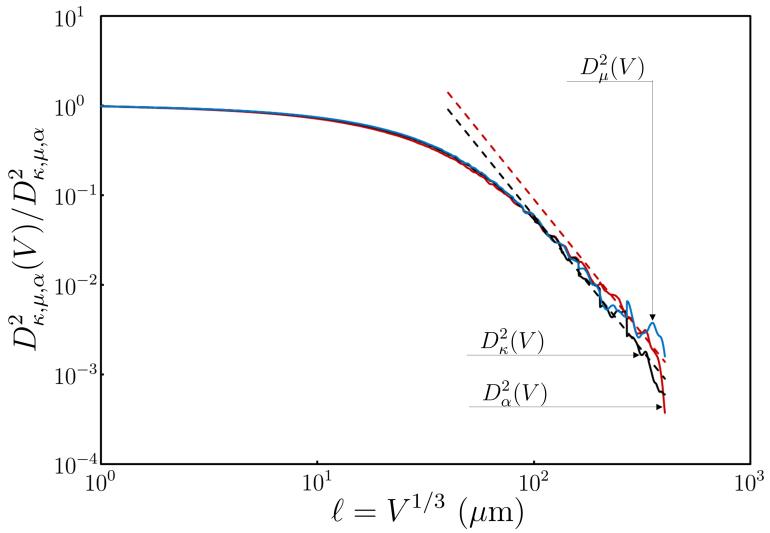

Figure 18: Variances $D^2_{\kappa,\mu}(\ell)$ and $D^2_{\alpha_V}(\ell)$ of the apparent elastic moduli and of the thermal expansion coefficient as a function of the length ℓ (µm) of a cubic volume of size $V = \ell^3$, in log-log plot. Dotted lines: fit $D^2_\kappa(\ell) \simeq (38/\ell)^3$, $D^2_{\alpha_v}(V) \simeq (45/\ell)^3$ for large ℓ.

versely isotropic. Despite this, numerical estimates lay in-between the two sets of bounds. They provide quite narrower estimates of the bulk modulus κ than bounds for the triclinic crystals.

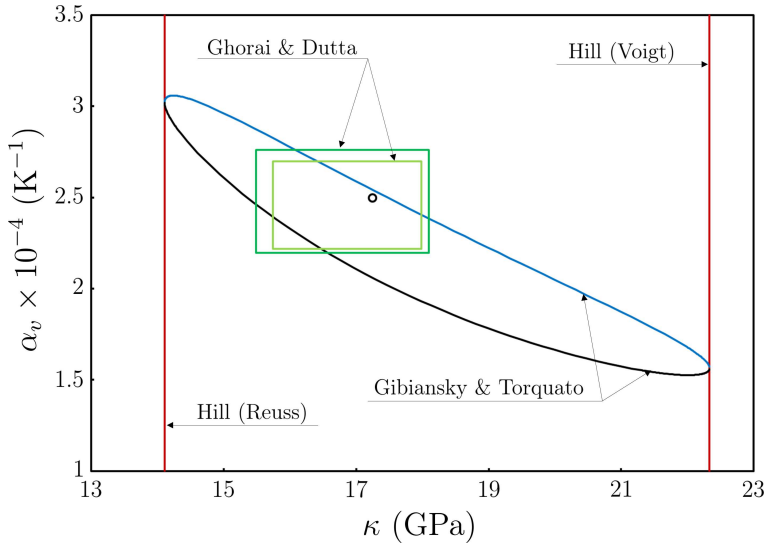

Figure 19: Bounds for the thermal expansion coefficient α_v and for the bulk modulus κ, represented in α_v-κ coordinates: Gibiansky & Torquato's bounds [31] for polycrystals with triclinic anisotropy (blue and black lines), Hill's bounds [34] for the bulk modulus (red vertical lines), "third-order" and "T-matrix" bounds (green) of Ghorai & Dutta [35] for polycrystals of crystals with hexagonal symmetries. The FFT results are marked by a black open dot.

6.6 Effect of a soft interphase

Our numerical result for the bulk modulus of the polycrystal, $\kappa = 17.2$ GPa, is much stiffer than experimental data, of 7.2 GPa. However, the softening effect of the binder, purportedly located in-between crystals, has not been taken into account in the FFT computations. In this section, we carry out additional computations that attempt to incorporate its effect on the effective proper-

ties.

The binder is not resolved in optical microscopy but its thickness is not larger than 300 nm, the diffraction limit of optical microscopy. With current FFT methods, the resolution required to incorporate the binder is unattainable and a different approach is sought for. Hereafter, we assume it is a higly-soft elastic layer of constant thickness ω located in-between crystals, with bulk modulus κ^{bind} and shear modulus μ^{bind}. When ω is much smaller than the size of the crystals, such interphases act as imperfect *interfaces* of the "soft type" [38, 39]. Vanishingly thin interfaces can not be handled in FFT computations. We therefore model the binder as an interphase with thickness $\omega = 4$ voxels $= 6.28$ µm and we choose:

$$\kappa^{\text{bind}} = 1.65 \text{ (GPa)}, \qquad \mu^{\text{bind}} = 0.67 \text{ (GPa)}.$$

The approach followed here is a crude simplification. First, contrary to the present model, the interphase thickness between crystals is likely to vary in the actual material. Second, the amount of porosity in the binder, not taken into account here, is unknown in the material.

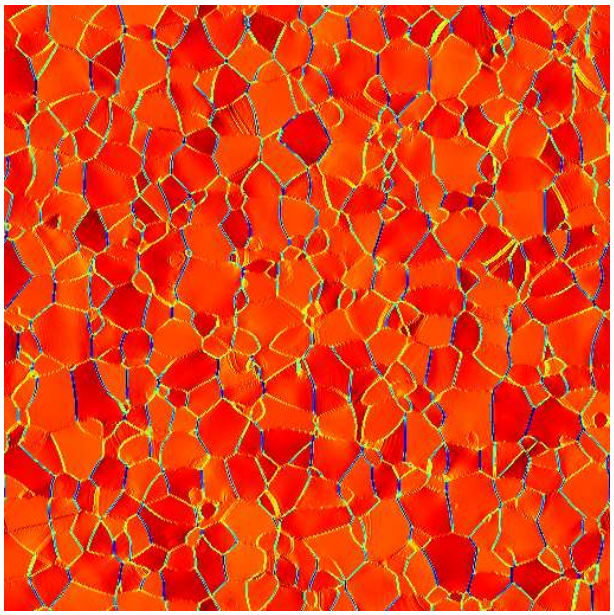

Figure 20: Longitudinal strain field ε_{xx} in polycrystal with binder. Applied thermal loading: $\Delta T = 1$; applied strain: $\overline{\varepsilon}_{ij} = 0$. Min. (blue): -8.7×10^{-4}. Max. (red): 2.0×10^{-4}. The x direction is vertical on the map.

Hydrostatic strain and thermal loadings are applied to the 512^3 voxels system with the soft interphase above. As an example, the strain component ε_{xx} is shown in Fig. (20) when thermal loading is applied. The strain field ε_{xx} is highly heterogeneous in the interphase. This is to be compared to the field histograms for the stress field (Fig. 21). Stress sollicitations for the mean stress component σ_m in the interphase and crystals are clearly separated. Compared with Fig. (14b), the level of stresses in the crystals are almost divided by two when an interphase is added.

The effective elastic moduli and thermal expansion coefficient read:

$$\begin{aligned} \kappa^{\text{int}} &= 7.93 \text{ (GPa)}, \quad \mu^{\text{int}} = 3.20 \text{ (GPa)}, \\ \alpha_v^{\text{int}} &= 2.42\,10^{-4} \ (K^{-1}). \end{aligned} \tag{26}$$

The values above are of the same order as experimental data, up to about 20%, except for the thermal expansion coefficient, for which, experimentally, $\alpha_v = 1.62\,10^{-4}$ K^{-1}. Among possible explanations for this discrepancy is the uncertainty on the elastic moduli of the monocrystal. Some authors [40] have recently calculated values for the elastic moduli of the monocrystal that are quite higher than the ones used in this study: $C_{11} = 78.4$ $C_{33} = 19.7$ $C_{66} = 29.7$ $C_{12} = 16.8$, some 20 to 37% higher than $C_{11} = 65.7$ $C_{33} = 18.3$ $C_{66} = 21.6$ $C_{12} = 18.5$ as used in this study. According to the results shown in Fig. (19), an increase of the overall elastic bulk modulus should decrease the thermal expansion coefficient.

Furthermore, another discrepancy appears in this model. Since the interphase width is 20 times higher in the FFT computations, much lower, and unrealistic local elastic moduli would be required in the binder to recover experimental data for the polycristal elastic moduli. Therefore, the soft-interphase model with constant thickness considered here is not sufficient. Instead, it should be modified, for instance by incorporating porosity. This

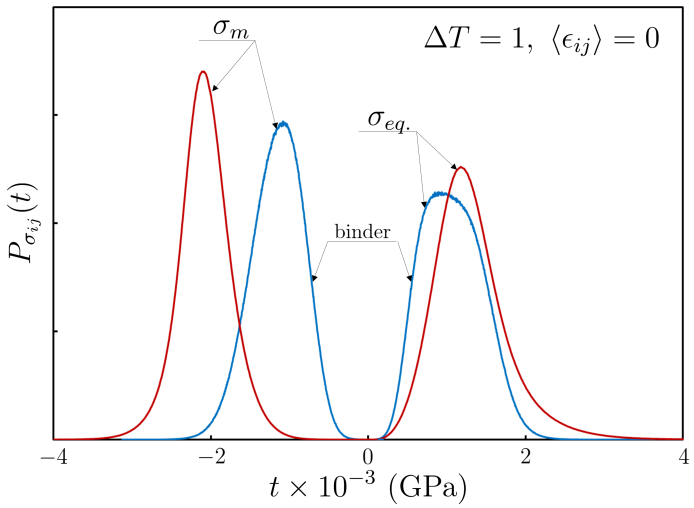

Figure 21: Mean and equivalent stress histograms related to Fig. 20. Blue: in the binder; red: in the crystals.

study, beyond the scope of the present work, has not been investigated further.

7 Conclusion and perspectives

The work presented here has demonstrated that it is possible to build a numerical upscaling tool with a detailed, though not yet fully realistic, description of the microstructure for the considered material. Classical microstructure models based on Poisson-Voronoï or Johnson-Mehl tesselations are insufficient to represent the wide grain size distribution, or granulometry, observed in the real material. More realistic models are recovered by modifying the germation rate of Johnson-Mehl tesselations. The first results have shown that input data are of the utmost importance, especially the anisotropic elastic constants for the TATB crystal. The combination of morphological tools and FFT-based numerical schemes is useful not as a predictive method that would replace experiments, but most importantly for the phenomenological understanding of the material's behavior.

The next tasks will be to improve the virtual microstructure model, which should incorporate the elongated character of the grains, their (sometimes strongly) non-convex forms, and eventually the presence of vestigial prills. The behavior of the binder is being characterized at present, at least in the glassy domain, i.e. below the glass transition temperature. An elastic-plastic constitutive model will be incorporated in the method, to describe the nonlinear response of the binder. Besides, it is planned to perform realtime observations at the microstructure level during a quasi-static compression experiment, in order to get data for validation purposes. Future work should extend the method by accounting for grain microcracking and plasticity, and for grain-binder debonding, in order to evaluate the effects of each potential mesoscale irreversible phenomena on the macroscopic (quasi-static) response of the material. For such purposes, it is expected that distribution tails of the local fields play a key role and should thus be studied thoroughly in future work.

Acknowledgements

We acknowledge the financial support of CEA. The tedious manual segmentation was carried out by Philippe Lambert, whom we thank gratefully. We wish also to thank Jean-Luc Brigolle, Didier Picart, Patrick Rey, Philippe Bortoluzzi and Alain Fanget for providing experimental mechanical data.

Appendix: Calculation of the thermal expansion tensor for the TATB single crystal

The goal of this Appendix is to derive the components of the thermal expansion tensor of the TATB single crystal from the variations of the lattice parameters with temperature given in [20], in the same coordinate systems than the elastic tensor given by [19]. The absolute reference frame is denoted by $(\mathbf{e}_1, \mathbf{e}_2, \mathbf{e}_3)$, where bold symbols are used for vectors. The crystallographic directions are denoted by $(\mathbf{e}_a, \mathbf{e}_b, \mathbf{e}_c)$. The lattice vectors are denoted by $(\mathbf{a}, \mathbf{b}, \mathbf{c})$, such that:

$$\mathbf{a} = a\mathbf{e}_a, \qquad \mathbf{b} = b\mathbf{e}_b, \qquad \mathbf{c} = c\mathbf{e}_c.$$

The crystallographic directions are such [19] that $\mathbf{e}_a = \mathbf{e}_1$, and that $\mathbf{e}_b$ lays in the $(\mathbf{e}_1, \mathbf{e}_2)$ plane, and the lattice angles

are defined by $\alpha = (\widehat{\mathbf{e}_b, \mathbf{e}_c})$, $\beta = (\widehat{\mathbf{e}_c, \mathbf{e}_a})$, and $\gamma = (\widehat{\mathbf{e}_a, \mathbf{e}_b})$. Then, one can write:

$$\mathbf{a} = a\mathbf{e}_1, \quad \mathbf{b} = b\left(\cos\gamma.\mathbf{e}_1 + \sin\gamma.\mathbf{e}_2\right),$$

$$\mathbf{c} = c\left(\cos\beta.\mathbf{e}_1 + \cos\theta.\mathbf{e}_2 + \cos\omega.\mathbf{e}_3\right),$$

where the angles θ and ω are such that:

$$\cos^2\beta + \cos^2\theta + \cos^2\omega = 1, \quad \cos\alpha = \cos\gamma\cos\beta + \sin\gamma\cos\theta.$$

Now, under the action of thermal strains, the components m_i of a lattice vector $\mathbf{m}$ transform as follows:

$$m_i(T) = \left[\delta_{ij} + \varepsilon_{ij}(T)\right] m_j(T_0),$$

which yield the following set of equations:

$$\begin{aligned}
a(T) &= \left[1 + \varepsilon_{11}(T)\right] a(T_0), \\
b(T)\cos\gamma(T) &= \varepsilon_{12}(T) b(T_0)\sin\gamma(T_0) \\
&\quad + \left[1 + \varepsilon_{11}(T)\right] b(T_0)\cos\gamma(T_0), \\
b(T)\sin\gamma(T) &= \varepsilon_{12}(T) b(T_0)\cos\gamma(T_0) \\
&\quad + \left[1 + \varepsilon_{22}(T)\right] b(T_0)\sin\gamma(T_0), \\
c(T)\cos\beta(T) &= \varepsilon_{12}(T) c(T_0)\cos\theta(T_0) \\
&\quad + \varepsilon_{13}(T) c(T_0)\cos\omega(T_0), \\
&\quad + \left[1 + \varepsilon_{11}(T)\right] c(T_0)\cos\beta(T_0), \\
\\
c(T)\cos\theta(T) &= \varepsilon_{12}(T) c(T_0)\cos\theta(T_0) \\
&\quad + \varepsilon_{23}(T) c(T_0)\cos\omega(T_0) \\
&\quad + \left[1 + \varepsilon_{22}(T)\right] c(T_0)\cos\theta(T_0), \\
c(T)\cos\omega(T) &= \varepsilon_{13}(T) c(T_0)\cos\omega(T_0) \\
&\quad + \varepsilon_{23}(T) c(T_0)\cos\theta(T_0) \\
&\quad + \left[1 + \varepsilon_{33}(T)\right] c(T_0)\cos\omega(T_0).
\end{aligned}$$

This system must be inverted to derive the six components of the thermal strains as functions of the six lattice parameters for each temperature value. Then, the thermal strains $\varepsilon_{ij}(T)$ are given by:

$$\varepsilon_{ij}(T) = \alpha_{ij}(T - T0)$$

which allows the six components of the thermal expansion tensor α_{ij} to be determined by a linear regression procedure.

References

[1] Rizzo, H. F., Humphrey, J. R., Kolb, J. R., 1981. Growth of 1,3,5-triamino-2,4,6-trinitrobenzene (TATB). II. Control of growth by use of high T_g polymeric binders. Propellants and Explosives, 6, 27–36.

[2] Maienschein, J. L., Garcia, F., 2002. Thermal expansion of TATB-based explosives from 300 to 566 K. Thermochimica Acta, 2002, 71–83.

[3] Thompson, D. G., Brown, G. W., Olinger, B., Mang, J. T., Patterson, B., DeLuca, R., Hagelberg, S., 2010. The effects of TATB ratchet growth on PBX 9502. Propellants, Explosives, Pyrotechnics, 35, 507-513.

[4] Gee, R. H., Maiti, A., Fried, L. E., 2007. Mesoscale modeling of irreversible volume growth in powders of anisotropic crystals. Appl. Phys. Lett., 90, 254105.

[5] Maiti, A., Gee, R. H., Hoffman, D. M., Fried, L. E., 2008. Irreversible volume growth in polymer-bonded powder systems: Effects of crystalline anisotropy, particle size distribution, and binder strength. J. Appl. Phys., 103, 053504.

[6] Demol, G., Lambert, P. Trumel, H., 1998. A study of the microstructure of pressed TATB and its evolution after several kinds of insults. 11$^{\text{th}}$ Int. Symp. on Detonation, Snowmass (CO), USA.

[7] Skidmore, C. B., Phillips, D. S., Idar, D. J., Son, S. F., 1999. Characterizing the microstructure of selected high explosives. EuroPyro 1999.

[8] Møller, J., 1992. Random Johnson-Mehl tessellations. Adv. Appl. Prob. 24, 814–844.

[9] Heinrich, L., Schüle, E., 1995. Generation of the typical cell of a non-Poissonian Johnson-Mehl tessellation. Commun. Statist. Stochastic Models 11:3, 541–560.

[10] Pineda, E., Bruna, P., Crespo, D., 2004. Cell size distribution in random tessellations of space. Phys. Rev. E, 70:6 066119.

[11] Jeulin, D., 2013. Random tessellations and Boolean Random Functions. Mathematical Morphology and its Applications to Signal and Image Processing, Lecture Notes in Comp. Sc., 7883, 25–36.

[12] Lantuejoul, C., 1977. Sur le modèle de Johnson-Mehl généralisé. Internal report N-514, École des Mines de Paris.

[13] Matheron, G. 1975. Random sets and integral geometry, Wiley, New-York.

[14] Castro, M., Domìnguez-Adame, F., Sánchez, A., Rodríguez, T., 1999. Model for crystallization kinetics: deviation from Kolmogorov -Johnson-Mehl-Avrami kinetics. Appl. Phys. Lett. 75, 2205.

[15] Ferenc, J., Néda, Z, 2007. On the size distribution of Poisson Voronoi cells. Physica A: Stat. Mech. and its Applications 385:2, 518–526.

[16] Farjas, J., Roura, P., 2008. Cell size distribution in a random tessellation of space governed by the Kolmogorov-Johnson-Mehl-Avrami model: Grain size distribution in crystallization. Phys. Rev. B 78:14, 144101.

[17] Jeulin, D., 1979. Morphologie mathématique et propriétés physiques des agglomérés de minerais de fer et du coke métallurgique. Thése de Docteur-Ingénieur en Sciences et Techniques Miniéres, Option Géostatique, Écoles des Mines de Paris.

[18] Cady, H. H., Larson, A. C., 1965. The crystal structure of 1,3,5-triamino-2,4,6-trinitrobenzene. Acta Cryst., 18, 485–496.

[19] Bedrov, D., Borodin, O., Smith, G. D., Sewell, T. D., Dattelbaum, D. M., Stevens, L. L., 2009. A molecular dynamics simulation study of crystalline 1,3,5-triamino-2,4,6-trinitrobenzene as a function of pressure and temperature. J. Chem. Phys., 131, 224703.

[20] Kolb, J. R., Rizzo, H. F., 1979. Growth of 1,3,5-triamino-2,4,6-trinitrobenzene (TATB). I. Anisotropic thermal expansion. Prop. Expl., 4, 10–16.

[21] Moulinec, H., Suquet, P., 1994. A fast numerical method for computing the linear and non linear mechanical properties of the composites. C.R. Acad. Sci., II 318:11, 1417–1423.

[22] Eyre, D., Milton, G., 1999. A fast numerical scheme for computing the response of composites using grid refinement. Eur. Phys. J. App. Phys. 6:1, 41–47.

[23] Vinogradov, V., Milton, G. W., 2008. An accelerated FFT algorithm for thermoelastic and non-linear composites. Int. J. Numer. Meth. in Engng 76:11, 1678–1695.

[24] Anglin, B. S., Lebensohn, R. A., Rolett, A. D., 2014. Validation of a numerical method based on Fast Fourier Transforms for heterogeneous thermoelastic materials by comparison with analytical solutions. Comput. Mat. Sci. 87, 209–217.

[25] Moulinec, H., Silva, F., 2014. Comparison of three accelerated FFT-based schemes for computing the mechanical response of composite materials. Int. J. Numer. Meth. Engng 97:13, 960–985.

[26] Michel, J. C., Moulinec, H., Suquet, P., 2000. A computational method based on Augmented Lagrangians and Fast Fourier Transforms for composites with high contrast. Comput. Model. Engng & Sc. 1:2 79–88.

[27] Michel, J. C., Moulinec, H., Suquet, P., 2001. A computational scheme for linear and non-linear composites with arbitrary phase contrast. Int. J. Numer. Meth. Engng 52:1-2, 139–160.

[28] Sauzay, M., Liu, J., Rachdi, F., Signor, L., Ghidossi, T., Villechaise, P., 2014. Physically-based simulations of the cyclic behavior of FCC polycrystals. Adv. Mat. Res. 891-892, 833–839.

[29] Willot, F., Abdallah, B., Pellegrini, Y.-P., 2014. Fourier-based schemes with modified Green operator for computing the electrical response of heterogeneous media with accurate local fields. Int. J. Numer. Methods in Engng 98:7, 518–533.

[30] Kanit, T., Forest, S., Galliet, I., Mounoury, V., Jeulin, D., 2003. Determination of the size of the representative volume element for random composites: statistical and numerical approach. Int. J. of Solids and Struct. 40:13, 3647–3679.

[31] Gibiansky, L. V., Torquato, S., 1997 Thermal expansion of isotropic multiphase composites and polycrystals. J. Mech. Phys. Solids 45:7, 1223–1252.

[32] Schapery, R. A., 1968. Thermal expansion coefficients of composite materials based on energy principles. Composite Materials, 2:3, 380–404.

[33] Rosen, B. W., Hashin, Z., 1970. Effective thermal expansion coefficients and specific heats of composite materials. Int. J. of Engrg. Sc. 8:2, 157–173.

[34] Hill, R., 1952. The elastic behaviour of a crystalline aggregate. Proc. Phys. Soc. A 65:5, 349.

[35] Ghorai, A. K., Dutta, T., 1995. Bounds on the effective thermal-expansion coefficient of a polycrystalline aggregate. J. Appl. Phys. 78:4, 2349–2354.

[36] Middya, T. R., Basu; A. N., 1986. Self-consistent T-matrix solution for the effective elastic properties of noncubic polycrystals. J. Appl. Phys. 59, 2368.

[37] Zeller, R., Dederichs, P. H., 1973. Elastic constants of polycrystals. Phys. Status Solidi B 55, 831–842.

[38] Benveniste, Y., 2006. A general interface model for a three-dimensional curved thin anisotropic interphase between two anisotropic media. J. Mech. Phys. Sol. 54:4, 708–734.

[39] Bövik, P. On the modelling of thin interface layers in elastic and acoustic scattering problems, 1994. Quart. J. of Mech. and App. Math. 47:1, 17–42.

[40] Valenzano, L., Slough, W. J., Perger, W. F., 2012. Accurate predictions of second-order elastic constants from the first principles: PETN and TATB. Shock Compression of Condensed Matter, AIP Conf. Proc. 1426, 1191-1194.